



LAWRENCE  
LIVERMORE  
NATIONAL  
LABORATORY

LLNL-TR-646844

# National Ignition Facility Quarterly Report

H. Robey, D. Casey, S. LePape, D. Shaughnessy

November 26, 2013

## Disclaimer

---

This document was prepared as an account of work sponsored by an agency of the United States government. Neither the United States government nor Lawrence Livermore National Security, LLC, nor any of their employees makes any warranty, expressed or implied, or assumes any legal liability or responsibility for the accuracy, completeness, or usefulness of any information, apparatus, product, or process disclosed, or represents that its use would not infringe privately owned rights. Reference herein to any specific commercial product, process, or service by trade name, trademark, manufacturer, or otherwise does not necessarily constitute or imply its endorsement, recommendation, or favoring by the United States government or Lawrence Livermore National Security, LLC. The views and opinions of authors expressed herein do not necessarily state or reflect those of the United States government or Lawrence Livermore National Security, LLC, and shall not be used for advertising or product endorsement purposes.

This work performed under the auspices of the U.S. Department of Energy by Lawrence Livermore National Laboratory under Contract DE-AC52-07NA27344.

# NATIONAL IGNITION FACILITY

**QUARTERLY  
REPORT**  
JULY-SEPTEMBER 2013



***Shock timing measurements and  
analysis in deuterium-tritium-ice  
layered capsule implosions on NIF***

***Development of the CD  
Symcap platform to study  
gas/shell mix in implosions at  
the National Ignition Facility***

***Indirect Drive Exploding  
Pusher on the NIF***

***Radiochemical determination of  
inertial confinement fusion  
capsule compression at the  
National Ignition Facility***

 Lawrence Livermore  
National Laboratory



This work performed under the auspices of the  
U.S. Department of Energy by Lawrence Livermore National Laboratory under Contract DE-AC52-07NA27344.

---

# Table of Contents

<b>Foreword .....</b>	<b>5</b>
<b>Shock timing measurements and analysis in deuterium-tritium-ice layered capsule implosions on NIF.....</b>	<b>7</b>
H. F. Robey	
<b>Development of the CD Symcap platform to study gas/shell mix in implosions at the National Ignition Facility.....</b>	<b>23</b>
D. T. Casey	
<b>Indirect Drive Exploding Pusher on the NIF.....</b>	<b>37</b>
S. Le Pape	
<b>Radiochemical determination of inertial confinement fusion capsule compression at the National Ignition Facility.....</b>	<b>43</b>
D. A. Shaughnessy	
<b>FY2013 NIF Shots- Summary Table.....</b>	<b>59</b>



# Foreword

This is the first issue of the National Ignition Facility (NIF) Quarterly Report. The report provides in-depth technical reviews of experiments performed on NIF supporting the Stockpile Stewardship Program in the areas of Inertial Confinement Fusion and High Energy Density Stewardship Science, as well as other National Security Applications and Fundamental Science. The report will also include articles on technology and science for advancing NIF as a facility. The goal is to provide a forum for presenting the world-class research being done on NIF in a timely fashion. This first issue contains four articles on results from recent experiments.

The first article reviews experiments on shock timing measurements in deuterium-tritium (DT)-ice layered capsule implosions on NIF. Ignition DT-layered targets are driven by a series of radiation driven shock waves of increasing strength. These shock waves compress and accelerate the capsule and DT ice layer fuel to spherically compress and heat them for creating the high density plasma conditions required to initiate DT fusion and burn. Controlling the strength and timing of the shock waves is important for optimally compressing the capsule and fuel to obtain ignition conditions. This article describes NIF experiments to measure the shock waves in the DT ice layers and adjust them to optimize the implosion.

The next article presents results from a set of experiments measuring the mix of capsule material into the hot fuel. Plastic (CH) capsules are made with a thin layer of deuterated plastic (CD) near the inner surface of the capsule. The capsules are filled with tritium and fusion yield from deuterium-tritium reactions is a measure of the amount of mix occurring in the implosion. The article describes results from experiments measuring mix using gas-filled capsules simulating ignition design targets.

The next article describes a platform being developed to calibrate in situ neutron diagnostics. The platform, called “indirect drive exploding pusher” (IDEP), uses a thin walled capsule filled with DT gas and near vacuum hohlraum to produce a relatively high-yield, low-areal density implosion. The hohlraum is driven with a simple two step laser pulse that produces a single shock implosion. The near vacuum fill of the hohlraum results in almost no laser cross beam energy transfer or laser-plasma interactions making them relatively simple to simulate. The single shock implodes the DT-filled capsule producing a low convergence, low areal density implosion that is a 14 MeV neutron source with low fraction of downscattered neutrons. This provides a good source for characterizing the system response of neutron diagnostics to 14 MeV neutrons with almost no downscattered neutrons.

The final article discusses a diagnostic technique to measure the neutron spectrum escaping from an imploded capsule and to potentially investigate nuclear cross sections. In indirect drive experiments, the Au hohlraum becomes activated from neutrons produced in the implosion. The composition of the activated products depends on the escaping neutron spectrum, or the relative number of downscattered neutrons. The diagnostic operates by collecting the target debris and counting the activated products. This article describes the technique for collection of the target debris and counting the activated products. Results are correlated with other nuclear diagnostics showing the sensitivity of the diagnostic to the neutron spectrum.





# Shock timing measurements and analysis in deuterium-tritium-ice layered capsule implosions on NIF

H. F. Robey<sup>1</sup>, P. M. Celliers<sup>1</sup>, J. D. Moody<sup>1</sup>, J. Sater<sup>1</sup>, T. Parham<sup>1</sup>, B. Kozioziemski<sup>1</sup>, R. Dylla-Spears<sup>1</sup>, J. S. Ross<sup>1</sup>, S. LePape<sup>1</sup>, J. E. Ralph<sup>1</sup>, M. Hohenberger<sup>2</sup>, E. L. Dewald<sup>1</sup>, L. Berzak Hopkins<sup>1</sup>, J. J. Kroll<sup>1</sup>, B. E. Yoxall<sup>1</sup>, A. V. Hamza<sup>1</sup>, T. R. Boehly<sup>2</sup>, A. Nikroo<sup>3</sup>, O. L. Landen<sup>1</sup>, M. J. Edwards<sup>1</sup>

1) Lawrence Livermore National Laboratory, USA 94551

2) Laboratory for Laser Energetics, Rochester, NY 14623

3) General Atomics, San Diego, CA

## I. Introduction

Inertial confinement capsule implosions on the National Ignition Facility (NIF) are performed using the indirect-drive concept [1], in which the energy of a temporally shaped laser pulse from 192 NIF beams is converted to thermal x rays in a cylindrical high-Z (Au or U) enclosure referred to as a hohlraum. Typical hohlraum dimensions for recent NIF implosions are 9.4 mm in length by 5.75 mm in diameter with the laser beams entering the hohlraum through two laser entrance holes (LEH) of diameter 3.1 mm. The x-ray radiation uniformly ablates the surface of a low-Z (CH or C) spherical ablator shell ( $r = 1.1$  mm), which surrounds a spherical cryogenic layer of solid deuterium-tritium (DT) fuel (70  $\mu\text{m}$  thickness,  $T = 18.7$  K,  $\rho = 0.255$  g/cm<sup>3</sup>) and central low-density (0.3 mg/cm<sup>3</sup>) DT gas fill. The hohlraum x-ray drive spherically compresses the ablator shell and fuel to create the high density and temperature plasma conditions required to initiate DT fusion reactions in the hot, compressed central fuel core.

A sketch of the hohlraum configuration and the driving laser pulse are shown in the inset of Figure 1(a).

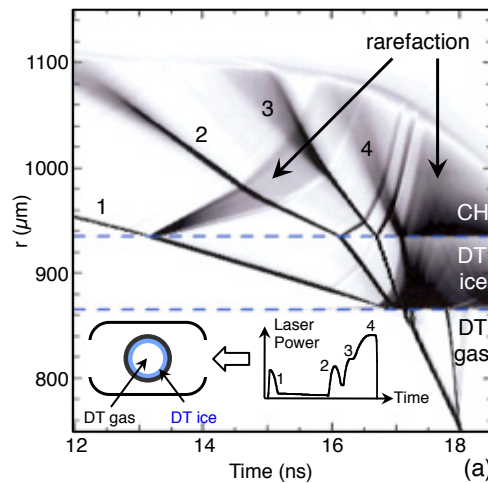


**Figure 1:** (a) Simulated shock trajectories in a DT-layered ignition capsule. Inset shows the geometry of a NIF ignition hohlraum and the laser pulse.

The laser pulse consists of four individual pulses of increasing energy, which drive a sequence of four shock waves into the ablator and DT fuel to compress it while maintaining low entropy and a low adiabat (ratio of fuel pressure to the Fermi degenerate pressure). Figure 1(a) shows simulated shock trajectories from a 1-D numerical simulation using the radiation-hydrodynamics code HYDRA [2]. The shocks and rarefactions are visualized by plotting the absolute value of the radial pressure gradient relative to the  $t=0$  material boundaries: CH ablator, DT ice, and DT gas.

The four shocks are tuned to traverse the DT ice layer sequentially, coalescing just after transit of the layer. Mistiming of the shocks results in increased fuel entropy and reduced compressibility, which severely degrades the prospects for ignition; see examples in [3].

To experimentally diagnose and adjust the strength and timing of these shocks, a modified hohlraum geometry is used as shown in the inset of Figure 1(b).

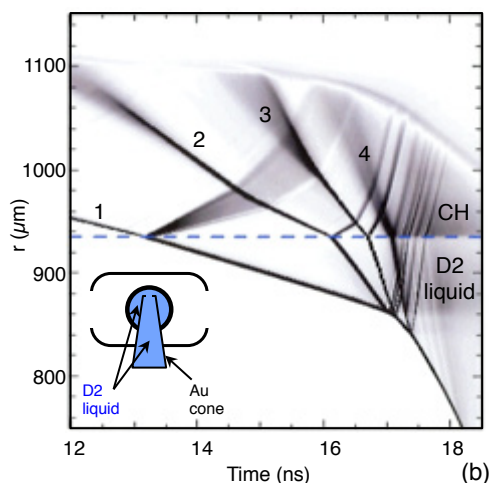


**Figure 1:** (b) Simulated shock trajectories in the “keyhole” tuning hohlraum. Inset shows Au diagnostic cone and ablator, both filled with liquid deuterium.

An Au diagnostic cone is added, penetrating both the hohlraum and capsule walls, to allow for the direct measurement of shock propagation in the capsule interior. Following the technique first described in [4], the capsule and Au cone are filled with liquid deuterium (D2) at  $T = 21.5$  K and  $\rho = 0.170$  g/cm<sup>3</sup> (replacing the DT ice and gas of an ignition capsule), and the Velocity Interferometer System for Any Reflector (VISAR) diagnostic [5, 6] is used to optically measure the velocity vs. time of the highly reflective leading shock front [7]. The shape of the D2-filled region is similar to that of an old-fashioned “keyhole,” hence this target has become known as the keyhole hohlraum. Initial experiments demonstrating the shock measurement technique and its application to shock tuning for directly driven implosions

on the OMEGA Laser Facility are reported in [8, 9]. Details of the modifications required for the higher power environment encountered in indirectly-driven implosions on NIF and initial tuning results for NIF ignition pulses are given in [10, 11].

Figure 1(b) shows the corresponding simulated shock trajectories in the keyhole target for the same laser drive as shown in Figure 1(a). Predicted shock trajectories are very similar, though not identical, in the ignition and surrogate tuning geometries, with the obvious exception of the rarefaction fan at  $t \approx 17$  ns that results as the first shock transits the strong density discontinuity at the DT ice-gas interface of an ignition target. This rarefaction is completely absent in the continuous D2-fill of the tuning target. Table 1 compares the predicted velocities ( $\mu\text{m}/\text{ns}$ ) of each shock between the D2 and DT-filled targets.

Shock number	Velocity in liquid D2	Velocity in DT ice	Difference (D2-DT)
1	18.4	17.5	0.9
2	35.0	33.4	1.6
3	67.8	63.7	4.1
4	100	90.5	9.5

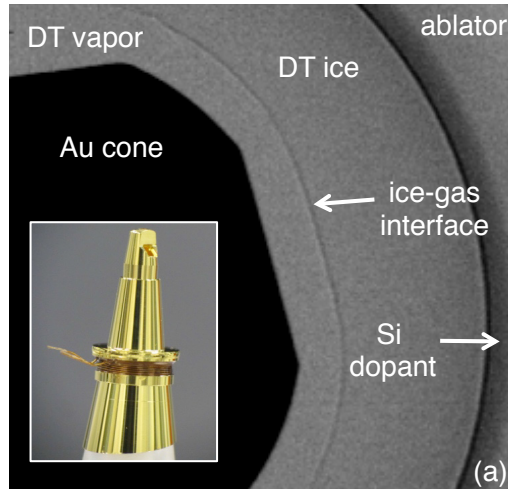
**Table 1** Comparison of shock velocities in liquid D2 vs. DT ice

The velocities measured in the less dense D2 liquid are slightly higher than in the more dense DT ice, as expected from the solution of the Riemann problem at the ablator-fuel interface [12]. These predicted differences are taken into account when applying a laser pulse tuned in a keyhole target to a layered DT implosion. Reference [13] presented the initial data assessing these surrogacy assumptions for the first three shocks. In this report, a more extensive discussion of the modified analysis procedures is given together with an extension of the experimental data to include the fourth shock.

## II. Material Surrogacy between D2 Liquid vs. DT Ice

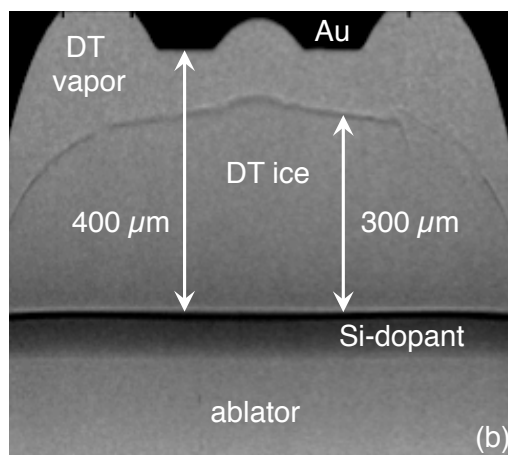
To quantify differences in shock strengths between liquid D2 tuning targets and layered DT ice ignition targets, the keyhole target was modified to allow for the growth of DT ice layers. As the inset of Figure 1(b) shows, the Au cone presents a severe perturbation to the capsule interior, precluding the growth of a uniform spherical ice layer. Simulations of the cryogenic thermal environment, however, show that with the addition of an external heater (resistive wire wrapped around the Au cone, just outside of the hohlraum as shown in the inset of Figure 2(a)), the isotherms in the DT at the cone tip, where the VISAR measurements are made, can be engineered to be locally spherical. The heater power required to grow reasonably uniform ice layers was  $\sim 10$  mW, a value which is comparable to the heat input used to control the sphericity of ice layers in ignition targets [14]; the heater input should therefore not perturb the hohlraum thermal environment. The mean layer thickness was controlled to an accuracy of  $< 1$   $\mu\text{m}$  by the initial gas volume that was injected into the target.

Figure 2(a) shows an x-ray radiograph taken through the LEH of a “thick” DT ice layer grown on NIF (shot N121101).



**Figure 2:** (a) X-ray radiograph of the capsule interior (shot N121101) showing the tip of the Au diagnostic cone, the Si-doped CH ablator, and the contour of a 300  $\mu\text{m}$  thick DT ice layer. Inset photograph shows the Au diagnostic cone with the additional wire-wrapped heater to control the isotherms.

The tip of the Au cone and the inner surface of the Si-doped CH ablator are clearly seen. The gap between these two surfaces was 400  $\mu\text{m}$ . The interface between the DT ice and the equilibrium DT vapor is visualized by x-ray refraction. The uniformity of the layer thickness is shown in Figure 2(b), where the image of Figure 2(a) is “un-folded” to visualize the ice layer thickness relative to the ablator inner surface.



**Figure 2b:** Unwrapped view of the DT ice layer of (a) showing ice thickness variation relative to the ablator inner surface.

The nominal thickness goal of this layer was  $300\text{ }\mu\text{m}$ , but considerable variation of the thickness is seen. Figure 2(b) shows nearly the full lateral extent of the layer from the center of the Au cone tip to the azimuthal location where the capsule contacts the cone. In this view, the flat portion of the Au cone tip appears as the curved region in the center. As the detailed shape of the heated Au cone determines the isotherms in the DT region, the ice layer thus formed follows the geometry of the Au cone to some extent.

The observed variation in the layer thickness does not affect the shock measurements, however, since as was seen in Figure 1, the entire shock velocity history is measured within  $200\text{ }\mu\text{m}$  of the ablator inner surface. A DT layer of thickness  $300\text{ }\mu\text{m}$  is therefore effectively infinitely thick and is used to provide a direct comparison of shock velocity histories with the continuous D<sub>2</sub>-filled tuning targets without any complication due to decompression of the ice layer. This configuration thus isolates the material surrogacy issue.

To study the effect of multiple shock release and recompression events from the DT ice to gas, layers of thickness corresponding to those used in ignition targets (nominal value  $70\text{ }\mu\text{m}$  [15]) were grown as well. Figure 2(c) shows an example of such a layer (shot N121108), where the thickness uniformity of the layer is again shown by unwrapping the image relative to the inner surface of the ablator.

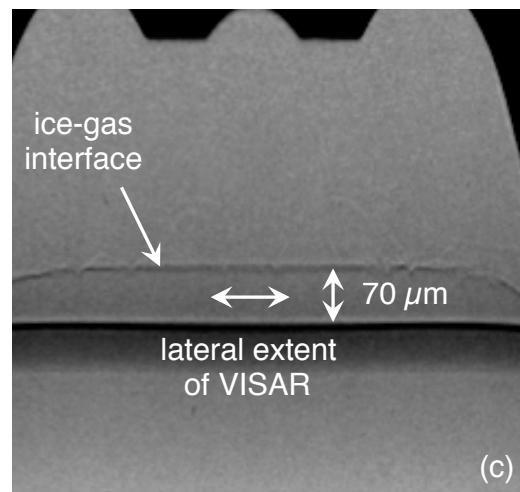


**Figure 2c:** Unwrapped view of a  $70\text{ }\mu\text{m}$  thick DT ice layer (shot N121108) showing reduced ice thickness variation relative to the ablator inner surface.

Due to the increased separation between the heated Au cone and the thinner layer, the thickness uniformity is observed to be considerably improved. This is important, as successive shocks will transit the full extent of this layer. The lateral extent of the VISAR measurements at the ablator inner surface is  $\sim 350\text{ }\mu\text{m}$ . The uniformity of the layer thickness over this field-of-view was measured to be better than  $1\text{ }\mu\text{m}$ . As will be shown in Section III, this small variation of layer thickness is seen in the VISAR data.

In reference [13], a comparison of the VISAR streaked interferometer data was shown for a standard, liquid-D<sub>2</sub>-filled target and a thick DT ice layer. It was shown that the measured difference in first shock velocity was in good agreement with the predicted values given in Table 1. The full VISAR shock velocity history over all 4 shocks is shown here in Figure 3(a).

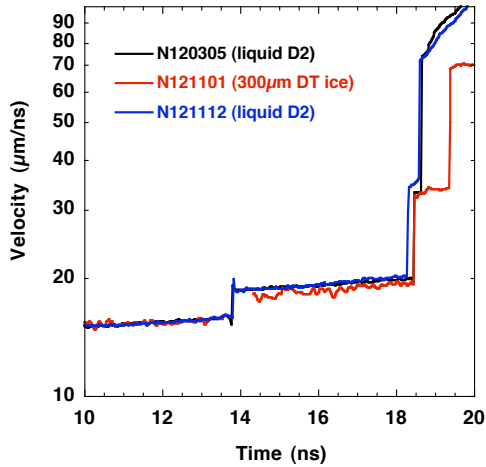


**Figure 3:** (a) Comparison of measured VISAR shock velocity histories between liquid D2 (shots N120305 and N121112 in black and blue, respectively) and a thick DT ice layer (N121101 in red). The fourth pulse in N121101 was intentionally delayed by 2 ns and is not seen.

The shock velocities measured in two liquid D2-filled shots (N120305 in black and N121112 in blue) are compared to those measured in a thick DT ice layered shot (N121101) in red. The corresponding laser pulses are shown in Figure 3(b) for these three shots.

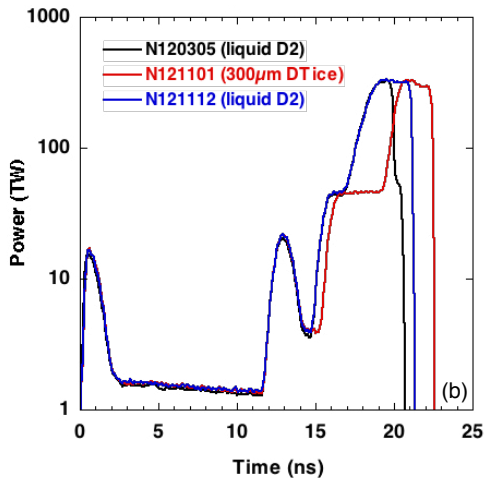


**Figure 3:** (b) Measured laser power histories corresponding to the three shots in (a).

For the two liquid-D2-filled targets, the laser pulses were identical for all four pulses with only the duration of the peak power portion of the pulse differing between the two. This part of the pulse has no effect on the measured shock timing,

and this difference is therefore indistinguishable by the VISAR measurements. The shock velocity histories in Figure 3(a) are very similar for these two shots, even though they were taken 8 months apart. This comparison of repeated shots serves to assess the repeatability of the measurements.

The laser pulse for the DT ice shot (N121101, red) was deliberately modified to ensure that all shock velocities were clearly seen (note that the merger of shocks 2 and 3 for the liquid D2 shots were rather closely spaced in time). The pulse is again identical through the second pulse. The launch of the third pulse, however, is delayed by 500 ps, and the launch of the fourth pulse was delayed by an additional 2 ns. This was done for initial experiments to avoid any complications with high-energy M-band pre-heat that is observed with the increasing power of the fourth pulse. The VISAR measured shock velocities of Figure 3(a) are identical in the ablator, as they should be. By comparison, the velocity in the DT ice is observed to be slightly lower than that in the liquid D2 throughout the entire time history, qualitatively consistent with the differences shown in Table 1.

Figure 4 shows a quantitative comparison of shock velocity metrics to evaluate the material surrogacy between liquid D2 and solid DT. In Figure 4, the velocity difference is shown in black from the measurements and in red from corresponding simulations. Shock velocity differences are shown for the first shock in the ablator (CH vel) and shocks 1-3 in the DD or DT (S1, S2, S3 vel).

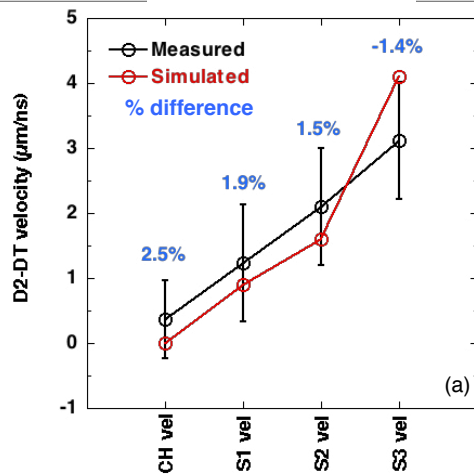


**Figure 4:** Quantitative comparison of shock velocity differences between liquid D2 and DT ice (measured difference in black, simulated difference in red). The relative percentage difference between data and simulation is listed in blue.

For both the measurements and simulations, the velocity difference increases with each successive shock, again in agreement with the differences predicted from Table 1. The measured and simulated differences agree to within the error bars of the VISAR measurements, which are taken as the sum of the individual error bars on the separate measurement in a DD and a DT-filled shot. The percentage differences between measurement and simulation (defined as the difference between measurement and simulation divided by the simulated value) are listed in blue above each velocity. The largest error of 2.5% is observed in the ablator, which is identical for both possible fuels. This is indicative of the absolute accuracy of this comparison. The percentage errors in the fuel are everywhere less than 2%, and decrease with each subsequent shock level.

The results of Figure 4 demonstrate that there is no material surrogacy error in the measurements relative to the predictions from simulation. Therefore, one can conclude that the database of shock timing measurements in liquid deuterium present no error in the tuning of DT ice layered ignition implosions. In the next Section, we address the geometric surrogacy issue.

### III. Geometric Surrogacy between Continuous D2 Liquid and DT Ice Layers

To explore the geometric surrogacy issue, we now look at the results from thin DT ice layers. Figure 5 shows a comparison of streaked VISAR interferometer data for (a) N121112 (liquid D2) and (b) N121108 (70 μm DT ice layer). Time runs from left to right, and lateral (bottom-to-top) motion of the interference fringes is directly proportional to the shock velocity with fringe motion upward indicating an accelerating shock. The relatively darker fringes at the top and bottom of each image are reflections of the VISAR laser from a stationary Au aperture at the tip of the Au cone as seen in Figure 1(b).

Fringe motion between these stationary references is due to reflections from the leading shock front in the fuel (D2 or DT). Discontinuities in the fringe positions indicate the arrival time of shocks. The first of these, labeled “1” and seen at 13–13.5 ns, is the time at which the first shock breaks out of the CH ablator into the fuel. Subsequent discontinuities indicate the time at which the increasingly stronger second, third, and fourth shocks overtake or merge with preceding shocks.

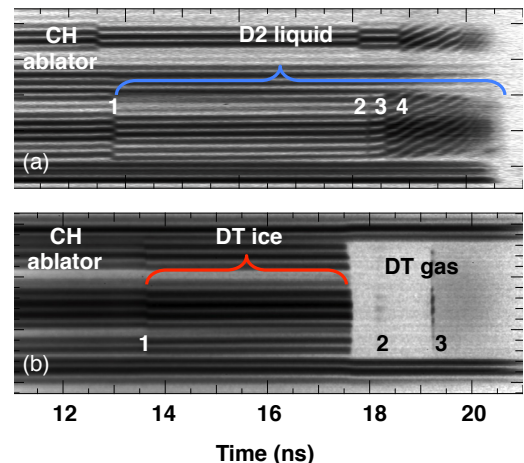


**Figure 5:** (a) VISAR streaked interferometer images for (a) shot N121112, a standard liquid D2-filled keyhole tuning target and (b) shot N121108, a 70 μm thick DT ice layer. Shock mergers 2 and 3 in (b) occur in the expanding DT gas region.



In Figure 5(a), the liquid D<sub>2</sub>-filled shot, all 4 shocks are seen, with the arrival time of shocks 2 and 3 adjusted to be close to that desired for optimal ignition tuning. Figure 5(b), a 70  $\mu\text{m}$  DT ice layer shot, shows several new features. The VISAR interferometer signal abruptly ceases at  $t \approx 17.5 \pm 0.07$  ns, as the first shock passes through the DT ice-gas interface (the spatial variation in breakout time is due to a small variation in the layer thickness as discussed earlier). The resulting rarefaction reflected from this interface as seen in Figure 1(a) generates pressure and density gradients in the expanding DT ice. As will be quantified later, the reduced pressure in the expanding ice drops below that required for reflectivity of the VISAR laser ( $\lambda = 660$  nm) [7]. As the second and third shocks traverse this decompressing ice region, they briefly recompress it to the pressure level required for VISAR reflection. This is seen in Figure 5(b) at  $t \approx 18.1$  and  $19.2$  ns as transient returns of VISAR reflectivity. The weaker signal from 19.2 to 20.5 ns is thermal emission from the stronger third shock; here the VISAR is functioning as a streaked optical pyrometer (SOP) [16, 17], recording thermal emission within the band-pass of the VISAR optical system. The fourth shock is not seen in Figure 5(b) as it was intentionally delayed to avoid complications with high-energy Au M-band (2-3 keV) radiation associated with the strong fourth pulse. The fourth pulse timing will be discussed later in this Section.

Figure 5(b) shows a comparison of the measured first shock velocities for these two shots, which both use the same laser pulse for the first two shocks. Small shot-to-shot power variations from the requested value in the early part of the laser pulse are accounted for by normalizing all shock velocity histories in the CH ablator. As was seen in Figure 4, the first shock velocity is again lower in the more dense DT ice by  $0.7 \mu\text{m/ns}$  relative to the D<sub>2</sub> liquid. This measurement is in excellent agreement with the predicted difference from numerical simulation ( $0.9 \mu\text{m/ns}$ ) as shown in Table 1.

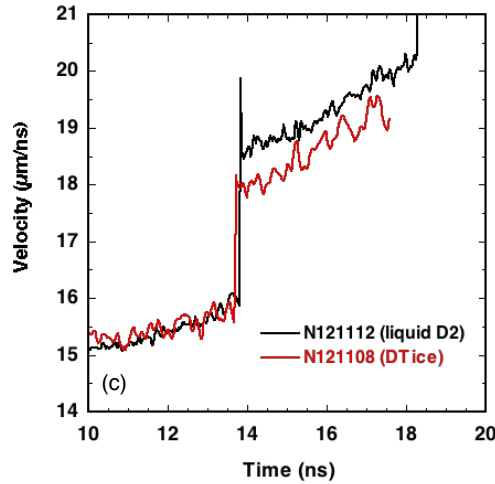


**Figure 5** (b) Comparison of measured shock velocity histories between liquid D<sub>2</sub> (shot N121112 in black) and a thin DT ice layer (N121108 in red).

The VISAR fringes abruptly cease in Figure 5(b) when the first shock breaks out of the finite thickness ice layer. Conventional VISAR velocity analysis can no longer be used beyond this time in these experiments. A wealth of additional information is available for the later time behavior, however, as will be discussed in the remainder of this section. The disappearance of the VISAR fringes at shock breakout can be used, for example, as a measure of early-time pre-heat. Integrating the shock velocity history in the DT ice from Figure 5(b) gives a measurement of the layer thickness of  $72.1 \mu\text{m}$ . This can be compared with the pre-shot x-ray measurement of the layer thickness such as that shown in Figure 2(c) of  $71.9 \mu\text{m}$ . These agree to better than the VISAR resolution. This comparison confirms that the ice layer is intact at least through the entire transit of the first shock with no premature decompression observed due to early-time pre-heat.

To analyze the data beyond the time of shock breakout, a new method of analysis is needed. The brief returns of VISAR reflectivity seen in Figure 5(b) provide timing information, but it is not clear how these can be compared to simulation to assess the level of agreement. We first must understand what these features correspond to and how they are generated. There is, for example, no information from the data on the radial location of these features in the imploding target, as one can no longer simply integrate the velocity history to obtain positional information. A new method that accounts for repeated periods of reflection and absorption of the VISAR laser is needed to quantitatively understand these features in the DT layered VISAR data.

To understand these features, we use the reported VISAR reflectivity measurements of Celliers [7], where it was shown that VISAR reflectivity in liquid D<sub>2</sub> exhibits a threshold response in both the electron density ( $n_e > n_{e,\text{crit}}$ ) and the pressure ( $P > 0.5$  Mbar). A metric for VISAR reflectivity from the simulations is therefore proposed as the following procedure: The electron density seen by the VISAR laser as it propagates through the fuel toward the shock front is quantified in the HYDRA simulations. When the probe laser reaches the critical density (satisfying the first VISAR reflectivity criterion), the pressure is recorded. Figure 6 shows contour plots from a 1-D HYDRA simulation to illustrate this procedure. Figure 6(a) is a contour plot of the material pressure as a function of Lagrangian radius and time. The Lagrangian radius gives the initial material boundaries and delineates the regions occupied by ablator, DT ice, and DT gas (separated by dashed horizontal lines). The trajectories of the 4 shocks are superposed on this contour plot. One can clearly see in Figure 6(a) a repeating sequence of shock compression and release events at the inner edge of the DT ice layer with a series of rarefaction waves propagating from the ice/gas interface upward toward the ablator.

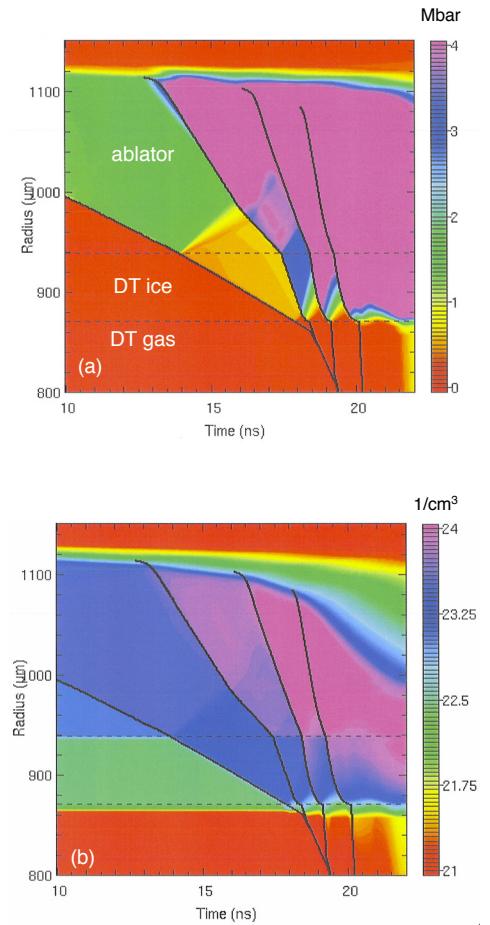
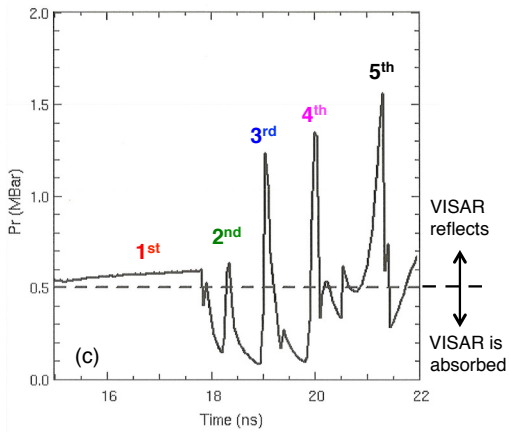


**Figure 6:** (a) and (b) Simulated contours of (a) pressure and (b) electron density plotted as radius vs. time for N130517.

Figure 6(b) shows the corresponding contour plot of the electron number density in the same format. The critical density for VISAR absorption or reflectivity is  $n_{e,\text{crit}} = 2.56 \times 10^{21} \text{ /cm}^3$ . In Figure 6(b), the color scale is plotted as  $\log_{10}(n_e)$ . The log of the VISAR critical density is 21.4 (the red-green boundary), which is located very near the inner edge of the DT ice layer.

The physical picture of the VISAR features labeled 2 and 3 in Figure 5(b) is now becoming clearer. These are not the locations of sequential shock mergers, but rather the time at which successive shocks recompress the releasing DT ice material to a pressure above the 0.5 Mbar threshold for VISAR reflectivity. Figure 6(c) plots this metric, the pressure at critical density, from the contour plots of Figure 6(a, b).

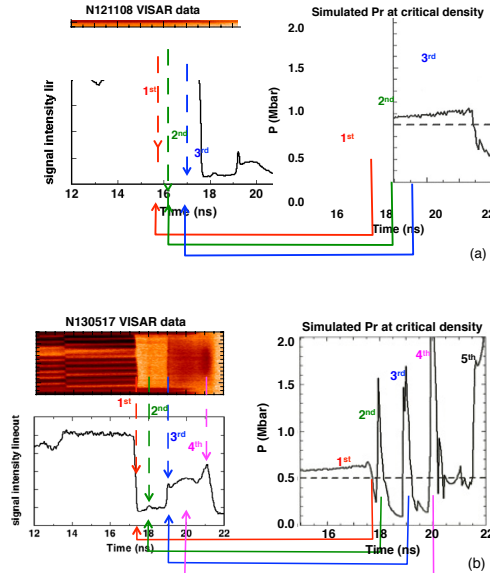




**Figure 6(c)** Simulated pressure at critical density metric showing predicted time history of VISAR reflection and absorption. Dashed line at  $P_r = 0.5$  Mbar is the threshold criterion for VISAR reflection from [7].

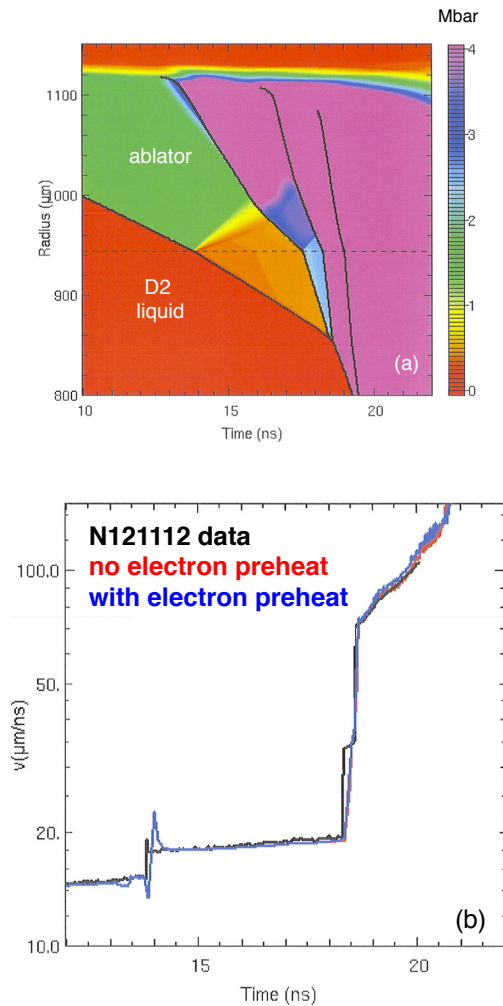
For the transit of the first shock, this metric shows a continuously increasing pressure of 0.5–0.7 Mbar due to the slightly accelerating first shock as it transits the ice layer. Upon shock breakout near 17.7 ns, the pressure abruptly drops as a rarefaction fan is reflected back into the ice layer. At  $\sim 18.2$  ns, the second shock recompresses this expanding DT and briefly brings the pressure (just barely) above the 0.5 Mbar threshold for reflectivity. The cycle then repeats. A now stronger rarefaction propagates outward toward the ablator (seen in Figure 6(a) as the rainbow fan-shaped region between shocks 2 and 3), and seen in Figure 6(c) as a significant drop in pressure at critical density to a value below the reflectivity threshold. The same process happens for the recompression caused by the third and fourth shocks. As Figure 6(a, c) show, a fifth shock is also predicted to occur.

Figure 7 applies this new VISAR analysis method to two DT layered keyhole shots to compare the transient reflection features observed after first shock breakout with predictions from simulation. Figure 7(a) shows a comparison for shot N121108 previously discussed in Figure 5(b).



**Figure 7:** (a) and (b): Comparison of measured vs. simulated shock timing for (a) a 3-shock system (N121108) and (b) a 4-shock system (N130517).

The VISAR streaked interferometer data is shown together with a lineout of the intensity taken through the vertical center of the data. The intensity is high for the first shock as it transits the DT ice, and then drops to a rather low value upon breakout. The two recompression features are seen in the lineout as transient increases in signal intensity. The simulated pressure at critical density is shown on the right-hand side of the Figure. The timing of first shock breakout, and second and third shock recompression is in excellent agreement with the data. It is important to point out that this simulation was based on a drive that was calibrated by matching to a continuous VISAR velocity measurement in a liquid-D<sub>2</sub>-filled shot (N121112), as shown in Figure 8. Figure 8(a) shows, for comparison, a contour plot of pressure indicating that the pressure in continuous D<sub>2</sub> remains above the 0.5 Mbar threshold at all times after passage of the first shock. Figure 8(b) shows a comparison of the measured (black) vs. simulated shock velocity history for this shot.



**Figure 8:** (a) and (b): Simulated pressure contours (radius vs. time) for N121112, a liquid D2-filled shot. (b) Comparison of measured (black) vs. simulated (red, blue) VISAR velocity histories showing excellent agreement for all 4 shocks. The red (blue) curve shows the velocity history from a simulation without (with) supra-thermal electron pre-heat in the fourth pulse.

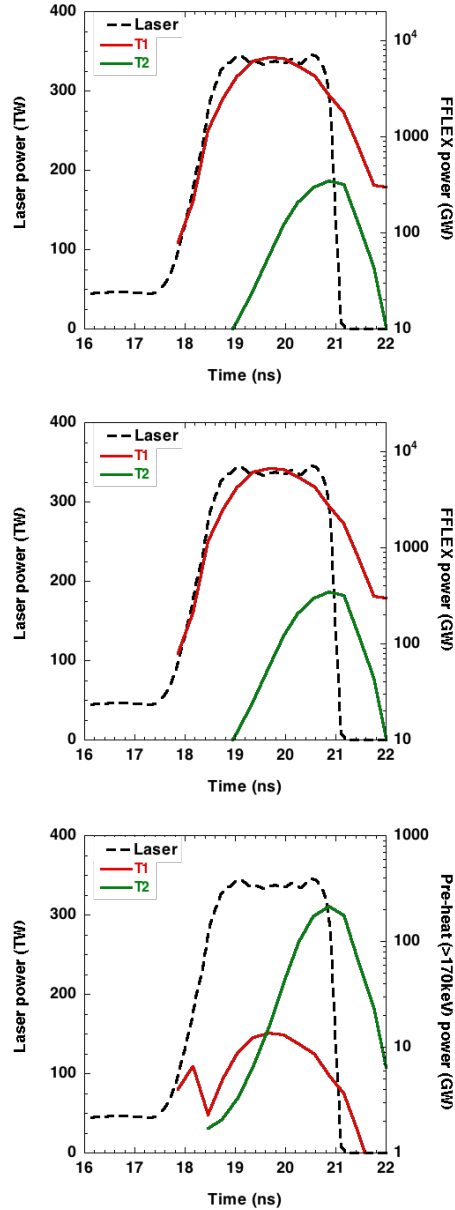
The red curve shows the velocity history from a “standard” simulation without supra-thermal electron pre-heat in the fourth pulse. The blue curve, to be discussed in the next Section, shows the shock velocity history from a simulation including supra-thermal electron pre-heat. Both simulations are in good agreement with the data, though the fourth shock velocity in the simulation including electron pre-heat is approximately 4% higher than without. The agreement in Figure 8 is obtained by adjustment of the drive and is used here purely as a normalization. The drive source used for the simulation of Figure 7, by contrast, has no additional adjustment. The level of agreement of the timing features in Figure 7 is therefore calibrated by reference to the tuned liquid D2 shot.

Figure 7(b) shows a second example of a similar 70 μm DT layer (shot N130517), but now with the fourth laser pulse advanced by 2 ns relative to that used in Figure 7(a). Again, an intensity lineout is taken from the data indicating the time of recompression features. The data now shows a fourth shock feature beginning at ~20.6 and peaking at 21 ns, whereas no such feature was observed in the VISAR data of Figure 7(a). The pressure at critical density metric is again shown on the right. The timing of first shock breakout and second and third shock recompressions is again in excellent agreement with simulation. The experimentally observed fourth shock feature, by contrast, is observed to be 600 ps later than in the corresponding simulation. This observation is significant, as the first three shocks show good reproducibility and good agreement with the data. The fact that only the fourth shock is in disagreement helps to rule out any possible systematic source of error. The fourth shock is, of course, the strongest shock, and its associated laser pulse introduces the possibility of additional physics that may play a role. In the next Section, a possible mechanism is proposed to explain this observed disagreement with the fourth shock timing. In the final Section, the consequences of this observation are discussed.

#### IV. Effect of Electron Pre-Heat on Fourth Shock Timing

There are several possible explanations for the observed discrepancy between simulated and observed fourth shock timing. Any mechanism that causes an additional expansion of the ice layer, for example, would delay the appearance of the fourth shock at the observed critical density for VISAR reflectivity. Possible mechanisms for such an effect include the DT equation of state (EOS) release behavior, mix at the DT ice/gas interface, x-ray pre-heat, or supra-thermal (or hot) electron pre-heat. Since the data and simulations seem to agree for the first three shocks, we need a mechanism that is specific to the timing of the fourth shock. Both EOS release and mix at the ice/gas interface will begin at first shock breakout, so these seem less likely. The current simulations routinely include M-band pre-heat, which is calibrated by Dante measurements [18], so that leaves hot electron pre-heat as perhaps the most likely mechanism.

Figure 9 shows the Filter-Fluorescer Experiment (FFLEX) [19] measurements for shot N130517 (DT layer of Figure 7(b)), which are used to infer the hot-electron pre-heat in NIF hohlraums. FFLEX on NIF consists of 10 time-resolved channels that measure hard x-ray Bremsstrahlung emission over a wide energy range. At any point in time, the FFLEX data can be well fit with a two temperature (T1, T2) Maxwellian distribution of supra-thermal electrons. Figure 9(a) shows the measured temporal history of the total hot-electron power (GW) for each of the two temperature components (T1 in red and T2 in green). Figure 9(b) shows the corresponding temperature of the two components to the fit. The low-temperature component, T1 (red), is  $\sim 30$  keV for  $t < 18.4$  ns and 18 keV thereafter. The high-temperature component, T2 (green) begins at about 19 ns and increases in temperature monotonically until the end of the pulse. Figure 9(c) shows the pre-heat power, defined as the power (GW) in the Maxwellian tail for electron energies  $> 170$  keV.



**Figure 9:** (a), (b), and (c): Comparison of measured laser power history for N130517 (black dashed) vs. (a) power, (b) temperature, and (c) pre-heat ( $>170$  keV) power from a time-dependent, two-temperature (T1, T2) fit to the hard x-ray measurements from the Filter-Fluorescer Experiment (FFLEX) diagnostic.

As discussed in [15], hot electrons in this energy range can penetrate the ablator and directly heat the DT fuel. Even though there is considerably more energy in the higher temperature (T2) component, it occurs too late to have a significant effect on the fourth shock timing that is observed by VISAR. Inclusion of the T2 component in the simulations has

little effect on the observed time of the fourth shock of Figure 7(b).

Inclusion of the lower-temperature (T1) component, however, does have an effect. The supra-thermal electron pre-heat is included in the HYDRA simulations using the non-local electron transport option, which is an extension to three dimensions of the method of Schurtz, Nicolai, and Busquet [20]. The model isotropically transports a Maxwellian distribution (or multiple distributions) of supra-thermal electrons that are added uniformly to the gas region outside of the capsule with a specified energy, temperature, and temporal history. In this case, we use the two-temperature power history of Figure 9(a) to model the distribution of hot-electron energies.

Figure 10 shows the effect on the simulated pressure contours and shock trajectories of adding the two-temperature Maxwellian hot-electron power history of Figure 9(a) to the simulations. Figure 10(a) shows the result with no electron pre-heat, while Figure 10(b) includes this additional energy source. In Figure 10(b), the solid lines show the simulated shock trajectories with pre-heat. The dashed curves in 10(b) show the trajectories for the non-pre-heated case for comparison. The first three shocks are essentially unchanged due to the addition of the hot electron source. The fourth shock, however, is delayed in time by approximately 300 ps, which is about half the discrepancy between measurement and simulation observed in Figure 7(b). The change in the shock trajectories can be seen in both the ablator and the DT fuel, but is most significant at the inside edge of the DT ice layer.

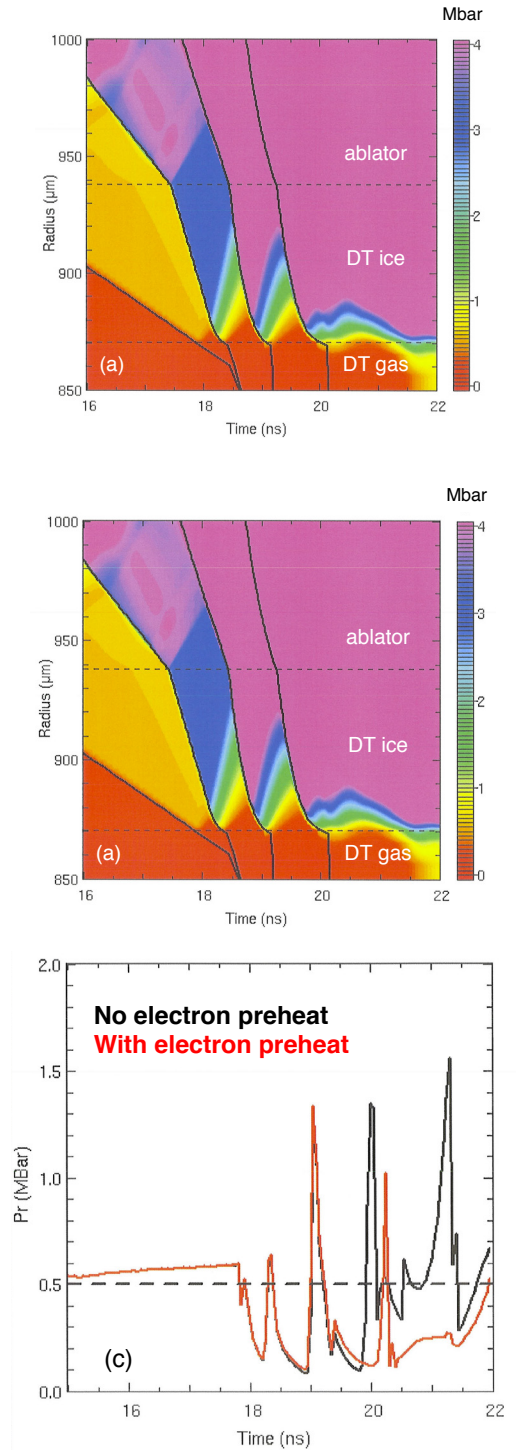


**Figure 10:** (a), (b), and (c): Simulated pressure contours (radius vs. time) with shock trajectories super-imposed. (a) no electron pre-heat and (b) with electron pre-heat from Figure 9(c). Dashed line in (b) shows shock trajectories from no-pre-heat case of (a). (c) Comparison of simulated pressure at critical density: (a) no electron pre-heat (black) and (b) with electron pre-heat (red).

Figure 10(c) plots the pressure at critical density from these two simulations: the one with no electron pre-heat (in black) and the one with added electron pre-heat (in red). The predicted timing of the first three shocks is completely unchanged, but the timing of the fourth is delayed by 300 ps. The predicted fifth shock feature is completely absent in the simulation that includes electron pre-heat. This change to the fourth shock timing is not as large as that observed in the data of Figure 7(b), but it does move the simulations into closer agreement with the observations. Increasing the pre-heat by a factor of two further increases the delay of the fourth shock to  $\sim 600$  ps, which is in reasonable agreement with the observations of Figure 7(b). This suggests that we need a slightly higher level of electron pre-heat than that measured by FFLEX to explain the VISAR observations.

The delay of the fourth shock timing shown in Figure 10(c) can be further understood by looking at the pre-heat expansion of the DT ice layer as shown in Figure 11. In these simulations, the DT ice layer was originally  $68\text{ }\mu\text{m}$  thick. The first three shocks compress the layer by more than a factor of 5 to  $\sim 12\text{ }\mu\text{m}$ . This is less than the full compression that would be obtained in a tuned ignition pulse, as the shocks are deliberately delayed in time to allow for complete diagnosis by VISAR.

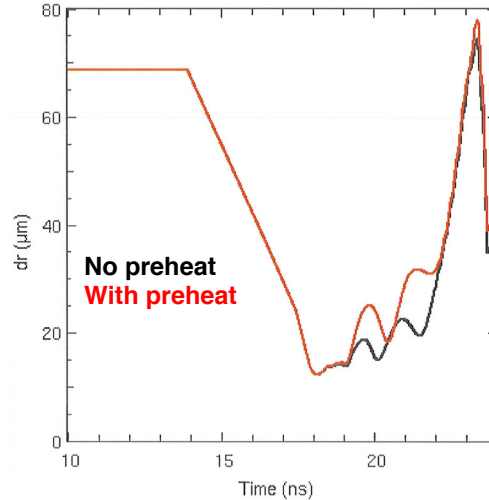


**Figure 11:** Temporal evolution of the simulated thickness of the DT ice layer with no electron pre-heat (black) vs. with electron pre-heat (red).

With electron pre-heat added, the layer expands by an additional  $5\text{--}10\text{ }\mu\text{m}$  during the decompression that occurs both before and after transit of the fourth shock, which was seen in Figure 10(c) to exit the layer at 20 ns (no pre-heat) and 20.3 ns (with pre-heat), respectively. This pre-heat induced expansion is a significant fraction ( $\sim 30\%$ ) of the compressed layer thickness and affects the implosion beyond the timing of the fourth shock. Figure 12, for example, shows the temporal evolution of (a) the fuel shell areal density ( $\rho R$ ) and (b) the absolute density in the hot-spot center. In both cases the density is reduced by  $\sim 30\%$  at peak compression. Increasing the pre-heat to twice the value inferred from FFLEX would reduce this to approximately half of the non-preheated value. This reduction in fuel  $\rho R$  and central compression is similar to that reported for a wide range of NIF ignition implosions in [21].



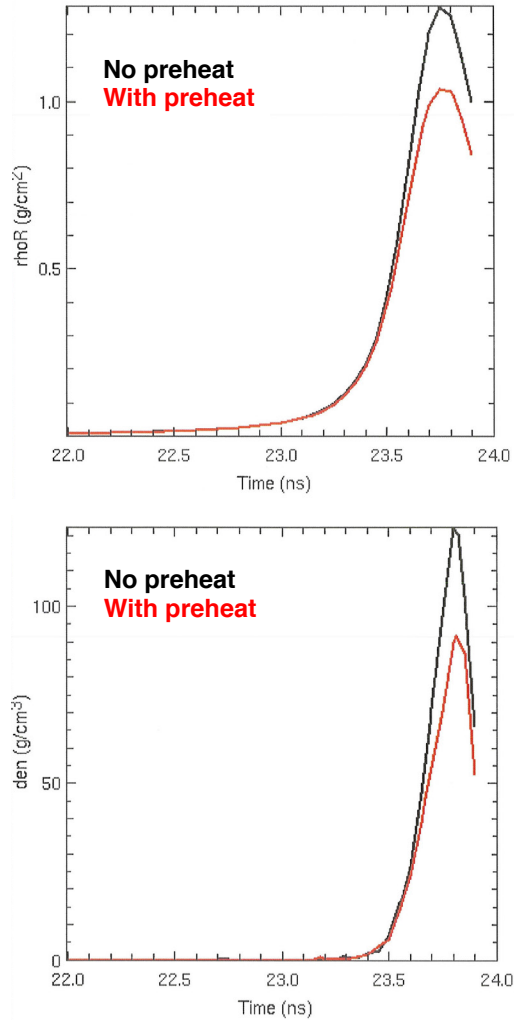


**Figure 12:** Temporal evolution of (a) fuel  $rR$  and (b) density at hot-spot center with no electron pre-heat (black) and with electron pre-heat (red).

## V. Summary and Conclusions

A new experimental capability for performing shock-timing experiments in DT ice layers has been presented. This capability has enabled an evaluation of both the material surrogacy between the different species (D2 and DT) with differing densities as well as the geometric surrogacy, which introduces an additional interface to the target structure.

Using thick DT ice layers allows one to isolate the material surrogacy issue with no complication due to the additional interface. The experiments show excellent agreement of the measured vs. simulated velocity differences between liquid D2 and DT ice for the first three shocks. We conclude that there is no material surrogacy issue, and that the simulations are correctly predicting the shock behavior.

Using thin DT ice layers enables an evaluation of the geometric surrogacy by introducing an additional material interface, which is repeatedly traversed by the successive shocks. A new method of analysis is introduced, where the pressure at VISAR critical density is used to provide a simulated metric of the VISAR timing signatures that are observed after breakout of the first shock from the ice layer. This method enables an assessment of shock timing in the presence of multiple shock release and recompression events. Comparison of this metric with VISAR data shows good agreement for the timing of the first three shocks, but a considerable discrepancy in the timing of the fourth shock.

Electron pre-heat is examined as a potential cause of the observed discrepancy in the fourth shock timing. A two-temperature Maxwellian supra-thermal electron source is added to the simulations, where the energy, temperature, and temporal distribution of this pre-heat source are taken from FFLEX measurements of the hot electron pre-heat observed at the leading edge of the fourth laser pulse. The simulated pressure at critical density metric shows that this pre-heat source delays the observation of the fourth shock feature, in better agreement with the data. Examination of the simulated DT layer thickness shows an increase of ~30% due to the added pre-heat. This pre-heat induced decompression persists in the implosions and correspondingly reduces the peak compression at stagnation by ~30%. This is in general agreement with the reduced pressures and densities (relative to simulation) that are inferred in a wide range of NIF ignition implosions.

The VISAR data and analysis techniques presented in this report provide a new capability for capsule-centric assessment of the effects of pre-heat on DT ice layers in ignition implosions. These observations add to the experimental constraints and may alter the previous understanding of implosion performance. Future work will apply these techniques to tuned ignition implosions to better constrain the implosion modeling.

## **VI. Acknowledgements**

This work was performed under the auspices of the Lawrence Livermore National Security, LLC, (LLNS) under Contract DE-AC52-07NA27344.

## VII. REFERENCES

- [1] J. D. Lindl *et al.*, *Phys. Plasmas* **11**, 339 (2004).
- [2] M. M. Marinak *et al.*, *Phys. Plasmas* **8**, 2275 (2001)
- [3] H. F. Robey *et al.*, *Phys. Plasmas* **20**, 052707 (2013)
- [4] D. H. Munro *et al.*, *Phys. Plasmas* **8** (5), 2245 (2001)
- [5] L. M. Barker and R. E. Hollenbach, *J. Appl. Phys.* **43**, 4669 (1972).
- [6] P. M. Celliers *et al.*, *Rev. Sci. Instrum.* **75**, 4916 (2004)
- [7] P. M. Celliers *et al.*, *Phys. Rev. Lett.* **84** (24), 5564 (2000)
- [8] T. R. Boehly, *Phys. Plasmas* **16**, 056302 (2009).
- [9] T. R. Boehly *et al.*, *Phys. Rev. Lett.* **106**, 195005 (2011)
- [10] H. F. Robey *et al.*, *Phys. Plasmas* **19**, 042706 (2012).
- [11] H. F. Robey *et al.*, *Phys. Rev. Lett.* **108**, 215004 (2012).
- [12] E. F. Toro, “Riemann Solvers and Numerical Methods for Fluid Dynamics,” Berlin: Springer Verlag (1999).
- [13] H. F. Robey *et al.*, *Phys. Rev. Lett.*, to appear (2013).
- [14] B. J. Kozioziemski *et al.*, *Fusion Sci. and Tech.* **59**, 14 (2011).
- [15] S. W. Haan *et al.*, *Phys. Plasmas* **18**, 051001 (2011).
- [16] R. J. Trainor *et al.*, *Phys. Rev. Lett.* **42**, 1154 (1979).
- [17] J. E. Miller *et al.*, *Rev. Sci. Instrum.* **78**, 034903 (2007).
- [18] E. L. Dewald, *et al.*, *Rev. Sci. Instrum.* **75**, 3759–3761 (2004).
- [19] E. L. Dewald, *et al.*, *Rev. Sci. Instrum.* **81**, 10D938 (2010).
- [20] G. P. Schurtz, Ph. D. Nicolai, and M. Busquet, *Phys. Plasmas* **7**, 4238 (2000).
- [21] C. Cerjan, P. T. Springer, and S. M. Sepke, *Phys. Plasmas* **20**, 056319 (2013).



# Development of the CD Symcap platform to study gas/shell mix in implosions at the National Ignition Facility

D. T. Casey,<sup>1</sup> V. A. Smalyuk,<sup>1</sup> R. E. Tipton,<sup>1</sup> J. E. Pino,<sup>1</sup> G. P. Grim,<sup>2</sup> B. A. Remington,<sup>1</sup> D. P. Rowley,<sup>1</sup> S. V. Weber,<sup>1</sup> M. Barrios,<sup>1</sup> R. Benedetti,<sup>1</sup> D. L. Bleuel,<sup>1</sup> E. J. Bond,<sup>1</sup> D. K. Bradley,<sup>1</sup> J. A. Caggiano,<sup>1</sup> D. A. Callahan,<sup>1</sup> C. J. Cerjan,<sup>1</sup> D. H. Edgell,<sup>3</sup> M. J. Edwards,<sup>1</sup> D. Fittinghoff,<sup>1</sup> J. A. Frenje,<sup>4</sup> M. Gatu-Johnson,<sup>4</sup> V. Y. Glebov,<sup>3</sup> S. Glenn,<sup>1</sup> N. Guler,<sup>2</sup> S. W. Haan,<sup>1</sup> A. Hamza,<sup>1</sup> R. Hatarik,<sup>1</sup> W. W. Hsing,<sup>1</sup> N. Izumi,<sup>1</sup> P. Kervin,<sup>1</sup> S. Khan,<sup>1</sup> J. D. Kilkenny,<sup>5</sup> J. Kline,<sup>2</sup> J. Knauer,<sup>3</sup> O. L. Landen,<sup>1</sup> T. Ma,<sup>1</sup> J. M. McNaney,<sup>1</sup> M. Mintz,<sup>1</sup> A. Moore,<sup>6</sup> A. Nikroo,<sup>5</sup> A. Pak,<sup>1</sup> T. Parham,<sup>1</sup> R. Petrasso,<sup>4</sup> H. G. Rinderknecht,<sup>4</sup> D. B. Sayre,<sup>1</sup> M. Schneider,<sup>1</sup> R. Tommasini,<sup>1</sup> R. P. Town,<sup>1</sup> K. Widmann,<sup>1</sup> D. C. Wilson,<sup>2</sup> and C. B. Yeamans<sup>1</sup>

1) Lawrence Livermore National Laboratory, Livermore, CA 94550

2) Los Alamos National Laboratory, Los Alamos, NM 87545

3) Laboratory for Laser Energetics, University of Rochester, Rochester, NY 14623

4) Massachusetts Institute of Technology, Cambridge, MA 02139

5) General Atomics, San Diego, CA 92121

6) AWE Aldermaston, Reading, Berkshire, RG7 4PR, United Kingdom

## I. Introduction

Hydrodynamic instabilities that grow during inertial confinement fusion (ICF) experiments, performed at the National Ignition Facility (NIF) [1], inject cold and high-Z material into the hotspot that can quench thermonuclear burn [2]. Turbulent instability growth during the deceleration phase of the implosion, also called mix, has been described as one of the key performance issues for cryogenic ignition experiments [3, 4]. Measurements of Ge doped capsule implosions have demonstrated that ablator material mixes through the ice layer and into the hotspot in cryogenic implosions [5]. Recently, measurements of X-ray yields relative to the neutron yields, in cryogenic DT experiments, have been used to infer the amount of ablator material that mixes into the hotspot. These data have shown that inferred mix mass has a strong inverse correlation with the overall yield [6]. It is therefore necessary to properly design targets that stay robust against

the deleterious effects of mix. However, first a predictive model, quantitatively benchmarked under similar conditions, is required.

A focused experimental platform called the “CD Symcap” platform has been designed, deployed, and used to validate mix models used to design experiments on the NIF [7]. The platform uses the same hohlraum, drive, and ablator as ignition targets but instead of a cryogenic DT ice layer, the “Symcap” capsule uses a surrogate plastic payload, in addition to the typical Si-doped plastic ablator. Originally designed to measure and tune hot-spot symmetry [8], the Symcap platform has been extended to study gas/shell mix by doping a thin layer of plastic with deuterium and filling the capsule with extremely pure tritium gas (<0.15 mole % deuterium). The CD Symcap experiments directly measure atomic-scale fuel/shell mix by observing the DT yield that occurs from tritium and deuterium, which were initially separated,

but have become turbulently mixed and heated. This technique has been used successfully before in direct drive laser experiments that used deuterated plastic layers (CD) with tritium filled [9] and helium-3 filled capsules [10, 11] at the OMEGA laser facility [12]. These CD Symcap experiments are nonetheless unique, as they represent the first time this technique has been used in indirect drive on the NIF [3]. In addition, these experiments are performed using actual ignition drives, targets (with surrogate plastic instead of ice), etc., to be as relevant as possible to ignition platforms.

The experimental target design is illustrated by Figure 13. The deuterated plastic layer is placed directly flush or recessed to up to 8  $\mu\text{m}$  from the gas/shell interface. The CD Symcap target is of the so-called “Rev5” ignition target design [2]. The Au hohlraum is 5.75 mm inner diameter by 9.43 mm tall (inside) with a laser entrance hole 3.373 mm in diameter. It is filled with  $0.96 \pm 0.01 \text{ mg/cm}^3$  of Helium gas to tamp Au-plasma in the hohlraum to improve irradiation symmetry, while also controlling laser plasma instabilities and cross-beam energy transfer [2, 13]. The entire target assembly including capsule and hohlraum is maintained at 32 K using the thermo-mechanical package designed and used for cryogenic DT experiments [4].

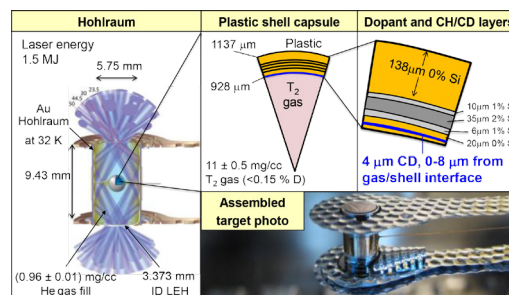


**Figure 13:** Schematic of indirectly driven CD Symcap target. Lasers irradiate the inside of a Au hohlraum, which produces x-rays that drive the capsule imploding inward. The capsules are filled with pure tritium gas and contain deuterated plastic layers at different distances from the gas/shell interface. The DT neutron yield of the imploded capsule is a direct measure of atomic scale fuel/shell mix. Included also in the bottom right panel is an assembled target photograph of shot N121119.

The capsule has an outer diameter of nominally 1137 mm with a total shell thickness of 209 mm. To shield the inner payload (usually DT ice but plastic in Symcaps) from the x-ray drive, and thereby reduce density discontinuity and instability [14], the plastic ablator is doped with three layers of graded Si (thicknesses and dopant concentration described in Figure 13). The inner plastic layer contains a mass-equivalent payload of plastic  $\sim 14 \mu\text{m}$  for a typical cryogenic ice layer (momentum balanced to achieve the same implosion velocity) accounting for the density of CH at  $1.06 \text{ g/cc}$  (at 32 K) and the solid DT density of  $0.255 \text{ g/cc}$  (the small density difference of doped CD layers in the payload are neglected). The CD layer is  $4 \mu\text{m}$  thick placed flush to the gas/shell interface or recessed up to  $8 \mu\text{m}$ .

The capsule is filled with  $11.1 \pm 0.5 \text{ mg/cc}$  of purified tritium gas corresponding to 4.0 atm at 32 K. An upper limit of 0.15 % (by atom fraction) residual deuterium contamination in the gas was determined by first filling the capsule, then retracting the gas from the fill system, and subjecting the sample to mass-spectrometry. Furthermore, several contamination shots were performed without CD layers to show DT yield from residual D in the gas (as will be discussed in more detail

later) and the results were consistent with D levels measured in the gas.

The laser drive was matched to cryogenic DT shot N111215, which utilized at 1.5 MJ laser pulse and a 436 TW peak power as shown in Figure 14. The hohlraum radiation temperature produced by the laser drive, as inferred by the Dante diagnostic, is also shown. The peak radiation temperature was consistently  $294 \pm 4$  eV for all shots in the campaign. As indicated on the figure, the x-ray bangtime (defined as peak x-ray self-emission brightness) occurred consistently  $\sim 1.5$  ns after the end of the laser drive at 22.5 ns.

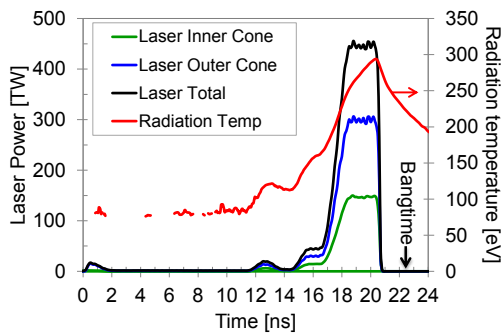


**Figure 14:** Measured laser pulse used to drive N130512 to 436 TW peak power, plotted as power as a function of time. All shots described here used the same laser pulse with excellent repeatability. Also shown is the measured hohlraum radiation temperature in eV, as determined from the DANTE diagnostic.

Despite careful matching of drive and target conditions to cryogenic DT experiments, there are important differences in CD Symcaps that must be considered in the context of mix. First, the imploded Symcap convergences are  $\sim 15$ , roughly a factor of 2 lower than typical cryogenic DT implosions. Because mix is very sensitive to convergence, this fact likely decreases the instability growth when compared to a cryogenic DT implosion. Second, the Atwood number at the gas/shell interface is higher, due to the larger density plastic payload (compared to DT ice), which likely leads to higher deceleration instability growth. Regardless of these differences, the data obtained from CD Symcaps provides direct and unambiguous measures of gas/

shell atomic mix that are essential for validating the mix models used to design and understand ignition experiments.

## II. Modeling CD Symcap experiments

### A. 1D hydrodynamic simulations using CALE/KL

The experiments described herein were designed using the arbitrary Lagrangian–Eulerian hydrodynamic code CALE [15, 16], which numerically solves the fluid equations to simulate the implosion hydrodynamics. Coupled to the KL turbulent mix model [16], CALE/KL includes predictions for atomic scale mix in CD Symcap implosions. The KL model describes the turbulence scale size and kinetic energy from multi-mode nonlinear Rayleigh–Taylor and Richtmyer–Meshkov instabilities in ICF implosions. With the constraints developed in the model, one free parameter  $L_0$  remains, which is the initial turbulence scale length. Figure 15 shows an example calculation using CALE/KL for a DT filled Symcap, designed to obtain high neutron yield required to employ the full nuclear diagnostic suite (useful for  $\rho R$  and nuclear gamma bangtime measurements). It is worth noting that the DT Symcap (illustrated in Figure 15a) is predicted to have similar overall hydrodynamic behavior as TT filled Symcap capsules, both with and without CD layers, because it was filled with the same initial fuel particle (fully ionized ion + electron) density. The predicted gas and shell density profiles at bangtime are shown in Figure 15b (calculated using 1D CALE/KL using an  $L_0 = 2000$  nm). The KL model allows the CH and DT to mix together. As the CH mixes into the hotspot, it radiates and cools the implosion. This energy loss degrades the core hotspot performance by effectively shrinking the burning volume. This is evident as the simulated burn profile ends where CH is mixing into the hotspot. This is in contrast to CD Symcaps, where the DT

neutron yield probes the atomic scale mix of T and D in this mixing region. Note also that the TT yield in CD Symcaps simultaneously probes the hotspot, which is degraded by both atomic scale mix and larger scale chunks and spikes of shell material.

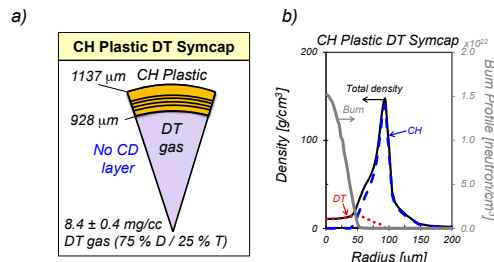
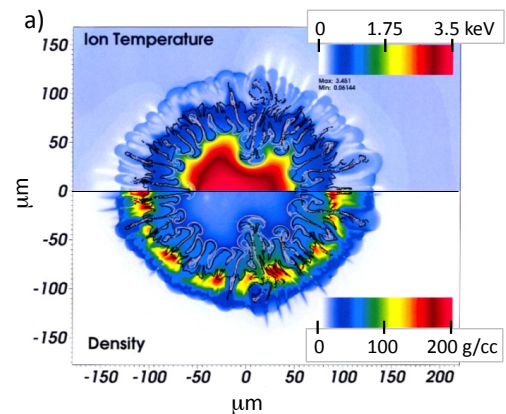


**Figure 15:** a) Capsule diagram for plastic DT filled Symcap implosion designed for high yield to employ the full suite of neutron diagnostics. This target is similar to the CD Symcap described in Figure 13, except that the gas is filled with DT and the capsule does not have a CD layer. b) Simulated 1D density profiles (black line) at bangtime for a plastic DT filled Symcap implosion calculated using the hydrodynamics code CALE/KL. Coupled with the turbulent diffusion model KL [16], these simulations include predictions of mix of the CH ablator (blue dashed line) material with the DT gas (red dotted line) material. The simulated burn profile is shown in grey.

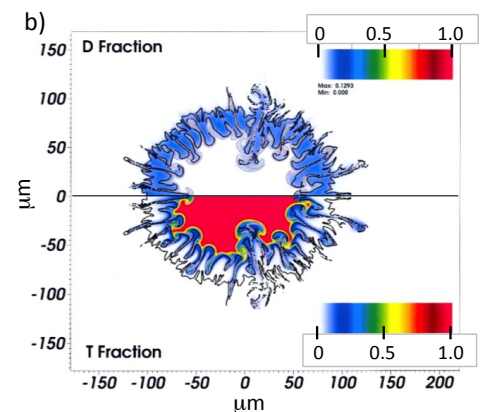
### III. 2D hydrodynamic simulations using ARES/KL

The radiation hydrodynamics code ARES was used to perform 2D simulations with an angular resolution of 1/8 degree [17]. These simulations capture low-mode (Legendre modes up to  $l=100$ ) hydrodynamic instabilities by initializing the problem with an imposed surface roughness (fill-tube, tent, and drive asymmetries are not included). High-mode turbulence leading to atomic mix is captured using the KL mix model.

Figure 16a shows the simulated ion temperature ( $T_i$ ) and density profile for 3× nominal surface roughness simulation (described later as the surface roughness required to match the platform performance, determined by the TT neutron yield).



**Figure 16:** a) 2D simulated  $T_i$  (top panel) and density (bottom panel) from ARES coupled with the KL mix model. Fingers and spikes move into the hot spot from growth seeded by outer capsule surface defects. This simulation used 3× the Rev5 surface requirement [18], which produced good agreement with the core TT neutron yield. b) Simulated deuterium fraction (top panel) and the tritium fraction (bottom fraction) for an inner surface CD layer implosion. c) Product of the simulated deuterium number density ( $nD$ ) and the tritium number density ( $nT$ ) for an inner surface CD layer (top panel) and a 2 μm recessed CD layer (bottom panel). The density product is the mix region where DT yield is produced in a CD Symcap (weighted toward the center by the temperature gradient shown in part a).



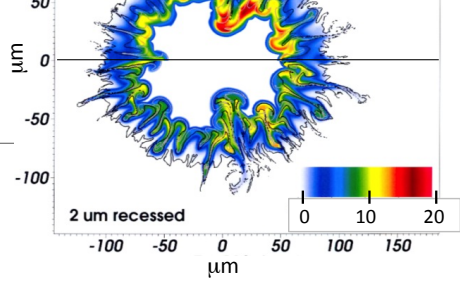


Figure 16b shows the deuterium and tritium fractions. The tritium fraction is high in the core region where the TT neutrons are produced ( $Y_{TT} \sim \text{tritium fraction squared}$ ). The deuterium fraction indicates the location of the CD layer including the mixing region where D and T can fuse. This figure indicates that D mixes into the core on the tips of fingers and spikes. This is better illustrated in Figure 16c, which shows the product of the deuterium

of the CD Symcap platform to study gas/shell mix in implosions at the National Ignition Facility

and tritium densities. The DT yield is produced on the outside of the central core in an annular mix region. Due to the strong radial temperature gradient, the DT yield is weighted toward the inner side of the mix region.

#### IV. Observed data from CD Symcaps

**Table 2** – Summary of observables from several TT filled CD Symcaps

NIF Shot Number	N121125	N130510	N130317	N130315	N130512	N130612	N130614
CD layer location	Inner CD layer	Inner CD layer	1μm offset CD	2μm offset CD	2μm offset CD	4μm offset CD	8μm offset CD
Ti (keV) [nToF]	2.0 ± 0.1	2.2 ± 0.1	2.1 ± 0.3	2.2 ± 0.2	2.6 ± 0.1	2.9 ± 0.1	3.4 ± 0.1
DT Yield	2.4 ± 0.07 e13	2.5 ± 0.08 e13	2.0 ± 0.06 e13	9.0 ± 0.3 e12	1.3 ± 0.04 e13	7.2 ± 0.3 e12	6.7 ± 0.3 e12
TT Yield	2.0 ± 0.2 e13	1.8 ± 0.2 e13	2.4 ± 0.2 e13	1.9 ± 0.2 e13	3.0 ± 0.3 e13	2.3 ± 0.2 e13	2.3 ± 0.2 e13
DSR (%)	1.2 ± 0.4	1.0 ± 0.1	1.2 ± 0.2	1.2 ± 0.4	1.0 ± 0.1	1.0 ± 0.1	0.9 ± 0.2
X Bangtime (ns)	22.50 ± 0.05	22.53 ± 0.02	22.55 ± 0.04	22.53 ± 0.03	22.53 ± 0.02	22.540 ± 0.01	22.56 ± 0.01
X-ray burn (ps)	307 ± 12	312 ± 30	309 ± 11	316 ± 9	320 ± 30	320 ± 15	325 ± 15
X-ray P0 (μm)	60.2 ± 4	55 ± 2	59 ± 3	53 ± 4	59 ± 2	63 ± 5	64 ± 5
X-ray P2/P0 (%)	13 ± 0.7	16 ± 1.1	1.3 ± 1.9	8.4 ± 2.6	15 ± 2.4	24 ± 4	23 ± 6
X-ray M0 (μm)		57 ± 8	65 ± 5	65 ± 6	58 ± 1.4		60 ± 3
X-ray M4/M0 (%)		1.9 ± 0.9	4.7 ± 3.6	4 ± 4	2.8 ± 0.3		3 ± 2

##### A. Neutron observations, TT yield, DT yield, and ion temperature

and is sensitive to the overall implosion performance. Quantitatively, the fusion yield of two arbitrary reactants, 1 and 2 (1 and 2 could be DT or TT), can be described by:

$$Y_{12} = \int \frac{n_1(\vec{r}, t) n_2(\vec{r}, t)}{1 + \delta_{12}} \langle \sigma v \rangle(\vec{r}, t)_{12} d\vec{r} dt, \quad \text{Eq. 1}$$

where  $n_1$  and  $n_2$  are the ion densities,  $\langle \sigma v \rangle$  is the fusion reactivity, and  $\delta_{12}$  is the Kronecker delta that accounts for double counting of identical reactants [19]. Following from Eq. 1, the DT neutron yield can be approximately evaluated in the mix region by:

$$Y_{DT} \approx n_D n_T \langle \sigma v \rangle_{DT} V_{mix} \tau_{mix} + Y_{DT-cont}, \quad \text{Eq. 2}$$

##### Eq. 2

where the  $V_{mix}$  is the burn volume of the mix region, is the  $\tau_{mix}$  is the burn width in the mix region and  $T_{DT-cont}$  is the yield from residual deuterium contamination in the tritium gas. A burn weighted metric of mix in the hot spot is then related to the product of  $\sim n_D V_{mix}$ . Correspondingly, the TT reaction yield from the tritium in the core (or hotspot) can be approximately evaluated by:

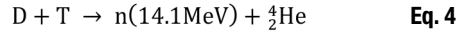
In a CD Symcap implosion, the DT fusion yield is a direct measure of D mixing into to the hot tritium core (along with trace D impurity in the tritium gas). Simultaneously, the TT fusion yield probes conditions of the hot core



$$Y_{TT-rx} \approx \frac{1}{2} n_{T-core}^2 \langle \sigma v \rangle_{TT} V_{core} \tau_{core}, \quad \text{Eq. 3}$$

where now the  $\tau_{core}$  and  $V_{core}$  are evaluated in the core.

The DT and TT fusion reactions both produce diagnostic neutrons, which are basis for the measurement of mix in the CD Symcap platform, as described by:



The DT reaction produces an alpha particle and a neutron at  $\sim 14.1$  MeV. The TT reaction produces an alpha particle and two neutrons per fusion reaction (note that unless otherwise specified, all discussion herein of the TT yield refer to the TT neutron yield, which is two times the TT reaction yield), creating a three-body neutron spectrum between 0-9.4 MeV. The exact details of the TT neutron spectrum are sensitive to the interactions between the emitted particles in the final state.<sup>20</sup> Knowledge of the TT neutron spectrum is important because it is required to connect observations, which are typically limited to a finite energy range due to detector cutoffs, to Eqs. 2 and 3. Calculating the TT neutron spectrum *ab initio* is extraordinarily difficult and work in this field is ongoing.<sup>21</sup> However, the TT neutron spectrum has been measured in a variety of accelerator and ICF experiments [22-26] and various models have been developed. In fact, the TT spectrum generated from these NIF experiments represents the highest quality produced to date, which has most recently been interpreted through R-matrix analysis [26]. Furthermore, the error in the TT yield is minimized as the TT neutron yield is obtained with six independent diagnostics, including three different nuclear techniques such as foil activation [17], neutron time of flight (nToF) [28, 29], and the magnetic recoil spectrometer (MRS) [30-32]. An estimate of the systematic error in the TT neutron yield, based on the comparisons of different models, is  $\sim 10\%$ .

An example set of measured neutron spectra are shown in Figure 17. These are

deconvolved spectra obtained using the nToF-SP diagnostic, located  $\sim 18$  m from the implosion [33]. This data was obtained in a pure tritium control shot without a CD layer (red), and a target with a CD layer flush on the gas/shell interface (blue). The DT yield is six times higher for the implosion with the CD layer, while the TT yield is nominally the same (see Table 2), demonstrating fuel/shell mix is pumping deuterium into the hotspot.

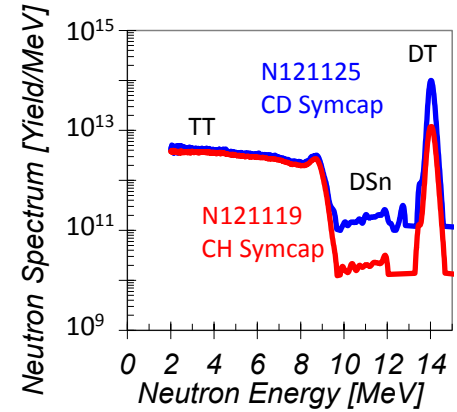


**Figure 17:** Time of flight measured neutron spectra (with the 18 m SpecSP detector) from a TT control capsule without a CD layer (N121119) and a CD Symcap with a CD layer flush with gas/shell interface (N121125). Immediately apparent is the stronger DT peak in the CD Symcap, which is caused by mix. Also shown are the down-scattered neutron (DSn) spectra, which are proportional to the product of the implosion  $\rho R$  and the DT yield. Note that the region between 12-13 MeV is poorly described due to a deconvolution artifact from the strong 14 MeV peak feature and is being investigated. The TT neutrons are apparent in the region below  $\sim 9.5$  MeV. The nearly overlapping TT-spectra show that these two implosions had very similar core performance.

The measured TT neutron yield for two control shots, or  $T_2/CH$  Symcaps, which were tritium filled capsules with CH shells (without CD layers) are shown by Figure 18a. The TT neutron yield for several CD Symcaps, as a function of the depth of CD recession from the gas/shell interface, is also shown. The TT yield is on average  $2.2 \times 10^{13}$  and reproducible to 20% within all shots on this platform.

1D CALE simulations with the KL mix model are shown as a black solid line in Figure 18a. As described earlier, CALE was used to design all experiments described herein. Clean calculations over predict the TT yield by a factor of 2-3; by increasing the initial mixing length scale (L0) the simulated TT yield was degraded to match the measured value. In these 1D simulations, the KL model simulates the effects of both, large scale (low mode) fingers and spikes, as well as small scale turbulence. Also shown are 2D ARES simulations with KL, where the outer surface roughness was scaled to match the TT neutron yield. A good match was found at  $3 \times$  the Rev5 surface roughness specification [18] (about 2 – 5 times the measured surface roughness). The overall TT performance is insensitive to small values of L0 (described later to match other observables) because low-mode instabilities dominate the yield degradation of TT coming from the hot core. The TT yield in both CALE and ARES is insensitive to the presence or recession depth of the CD layer, in agreement with observation. This is because the difference in CD density (1.14 g/cc at 32 K) compared with CH (1.06 g/cc at 32 K) is minimal, implying very similar expected hydrodynamics.

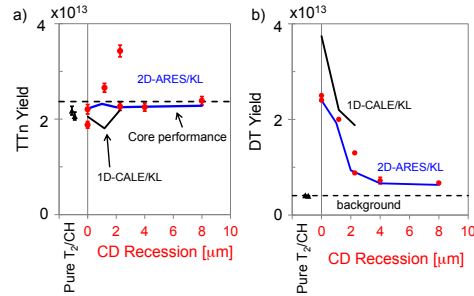


**Figure 18:** a) Measured TT neutron yield for two tritium-filled CH Symcaps, which characterized the D contamination background, and several CD Symcaps. The CD Symcap TT yield is plotted as a function of the recession depth of the CD layer from the gas/shell interface. As expected, no trend with recession depth is observed. Simulated CALE and ARES yields are also shown. The simulations have been adjusted to match the TT yield. b) Measured DT yield for two TT CH Symcaps and several CD Symcaps. The DT yield from the TT CH Symcaps characterizes the background from D contamination ( $<0.15\%$  D) in the tritium and the core performance, while the DT yield from the CD Symcaps is from mix.

The DT neutron yield is shown in Figure 18a for two control (contamination D only, no CD layer) TT Symcaps, and several CD Symcaps. The DT yield for the CD Symcaps is plotted as a function of the recession depth of the CD layer from the gas/shell interface. The DT yield drops with increasing recession because the mix yield is dominated by material mixing in from the inner part of the shell. Although not shown, a 75/25 DT Symcap was also imploded and produced  $6.8 \pm 0.2 \times 10^{14}$  DT neutrons with a down-scattered neutron ratio (related to areal density and defined as neutron yield 10-12 MeV over 13-15 MeV) [32, 34, 35] of  $1.1 \pm 0.1\%$ . Figure 19a provides the DT neutron to TT neutron yield ratio (DT/TT), a metric that is related to mix. Interestingly, even though there is some scatter in the TT and DT neutron yield for identical shot repeats (at 0 and 2 mm recession), the DT/TT remains very repeatable.

Figure 18b and Figure 19a also show the DT yield and DT/TT yield ratio predictions, respectively, from the 1D CALE/KL

calculations with the parameter  $L_0$  adjusted to match the TT yield. In this case the DT yield is over estimated by a factor of 1.5–2. This may be because the CALE/KL mix model is accounting for fingers and chunks that do not produce atomic scale mix that is required to generate DT neutrons. There may also be a diffusion time associated with mixing of D and T is that is slower than currently predicted. These possibilities are under investigation. 2D ARES/KL simulations are also shown, where the surface roughness has been adjusted to 3x the NIC specified acceptable value [18] to match the TT yield, and the  $L_0$  in the KL model is adjusted to 0.1 nm to match DT yield for the capsule with the CD layer on the gas/shell interface. With those two parameters fixed, the ARES/KL calculations provide a reasonable match to the measured DT neutron yield as the CD layer depth is varied.

$T_i$  is inferred through the Doppler broadening of the 14.1 MeV neutron peak, measured with the nToF suite [28, 29] and MRS diagnostics [30] and represents a burn-averaged DT- $T_i$ . The observed  $T_i$  produced in a DT Symcap filled to 75% deuterium and 25% tritium is shown in Figure 19b along with two TT Symcaps, where the DT neutrons are produced by contamination D in the core gas. The TT Symcaps are in excellent agreement with the core temperature of the DT Symcap indicating similar burn conditions at ~3.5 keV. Figure 19b also shows the  $T_i$  measured from the mix region from several CD Symcaps. The  $T_i$  for the CD Symcap at the gas/shell interface is ~2 keV, much lower than the core temperature, because CD-shell mix comes from deuterium on the outside, cooler, part of the core.  $T_i$  increases from ~2 keV and approaches the core temperature of ~3.5 keV, with increasing depth of recession, because the relative contribution of the cooler mix yield decreases to that of the D contamination yield in the core. A summary of all yields and  $T_i$  is provided in Table 2.

Figure 19b shows CALE and ARES predictions for the observed  $T_i$  for the CD

Symcap implosions, as a function of the depth of recession. Both codes capture the  $T_i$  of the CD Symcaps at all recessions well, indicating that the radial location and extent of the mix (because temperature is function of radius) is well understood.

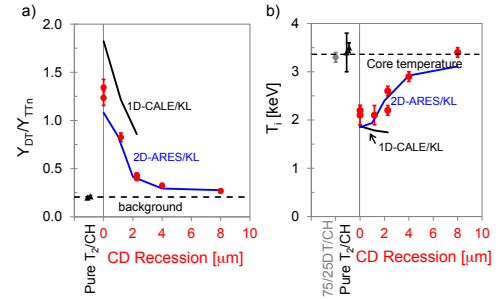


**Figure 19:** a) Measured TT to DT neutron yield ratio for CD Symcaps, as a function of the recession depth for the CD layer from the gas/shell interface. The DT/TT yield ratio, a measure of the atomic mix in the core, decreases as a function of recession depth demonstrating sensitivity of the platform to gas/shell mix. b) Measured  $T_i$  determined by the Doppler width of the DT neutron peak for a DT Symcap, two pure TT Symcaps (DT neutrons are produced with D contamination in the  $T_2$  gas), and several CD Symcaps. The  $T_i$  of the DT and TT Symcap characterize the burn averaged core temperature. The CD Symcaps are plotted as a function of the recession depth of the CD layer from the gas/shell interface. As the recession depth increases,  $T_i$  approaches the core value because less neutrons are produced in the cooler mix region. Simulated ARES ion temperatures are in good agreement with observations.

An approximate burn-averaged mix mass estimate can be extracted from the data by combining Eq. 2 and Eq. 3. This can be accomplished by assuming an isobaric relationship between the core and burning mix regions and recasting Eq 3 into the form for the TT neutron yield (note that there are two neutrons per TT reaction) as a function of the plasma pressure:

$$Y_{TT-n} \approx \left( \frac{P}{2 T_{core}} \right)^2 \langle \sigma v \rangle_{TT} V_{core} \tau_{core} \quad \text{Eq. 6}$$

By next assuming an ideal equation of state, the TT neutron yield can be used to determine the tritium density in the mix region and substituted back into Eq 2. By neglecting the CD contribution to the pressure in the mix region (expected to be a fairly reasonable assumption



in the burn-weighted part of the mix region), the inferred mix mass takes a particularly simple form. Assuming the same CD ratio as in the pre-shot shell (1.35 D/C), evaluating constants, and solving for the mix mass leads to the following relationship:

$$m_{CD} \sim 1.2 \times 10^{-7} \frac{T_{mix}}{T_{core}} \frac{\sqrt{\tau_{core}}}{\tau_{mix}} \frac{\sqrt{\langle \sigma v \rangle_{TT-core}}}{\langle \sigma v \rangle_{DT-mix}} \frac{Y_{DT}}{\sqrt{Y_{TT}}} R^{3/2}$$

#### Eq. 7

where the mass is in ng, the reactivity is in  $\text{cm}^3/\text{s}$ , the burn widths  $\tau$  are in ps, the yields  $Y_{DT}$  and  $Y_{TT}$  are in units of  $10^{13}$  neutrons,  $R$  is the average core radius in  $\mu\text{m}$ , and  $T$  is the temperature. The inferred mix mass from Eq. 7 is about  $\sim 750$  ng from the inner surface CD layer shots and drops swiftly with recession of the layer, as evident in Figure 19. This implies that most of the mix occurs with material on the inner surface of the shell during the deceleration phase of the implosion. It is possible that additional contributions and/or seeds come from ablation front instabilities driven during the acceleration of the shell. The exact role of ablation front instability will be the subject of future studies with high convergence implosions, the addition of multiple spectroscopic tracers (Ge and Cu), and with further recessed and thicker CD layers.

### B. Simultaneous core and mix neutron imaging

The neutron imaging system (NIS) is also used to image the TT core burn and DT mix burn regions simultaneously by time-gating two NIS CCD cameras, which are normally timed to look at DT and down-scattered neutrons. During shot N121125 (inner layer CD Symcap) NIS was configured to look at 13-17 MeV for DT and 6-12 MeV (TT) and the resulting images are shown in Figure 20. A method to infer mix mass from the difference in the sizes of the two burn regions is currently under development [36]. Preliminary estimates are consistent with the yield method described earlier.

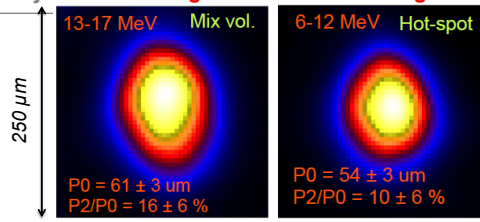


**Figure 20:** Energy gated neutron images, viewed from the equator, of a CD Symcap with the CD on the inner layer of the gas/shell interface (N121125). Two neutron cameras were timed to observe the DT neutrons (13-17 MeV) and TT neutrons (6-12 MeV) simultaneously from the same implosion. The DT burn is slightly larger than the TT burn consistent with the picture of annular mix region burning on the outskirts of a central core.

### C. X-ray core imaging

The hotspot shape was observed using time-gated X-ray framing cameras that are configured for the hot-spot self-emission. These measurements, performed with the GXD and hGX instruments [37, 38], show that hotspot shape implodes into a 55-60  $\mu\text{m}$  radius hotspot with a typically prolate shape (see Table 2). The X-ray bangtime obtained from the framing camera images is 22.5 ns for this platform in good agreement with CVD based southpole bangtime [39] and streaked SPIDER instruments [40]. Additionally, neutron bangtimes are  $\sim 22.5$  ns as recorded with the pTOF diagnostic [41]. Interestingly, these X-ray images also show brightly radiating objects traversing through the hotspot, as shown in Figure 21. These objects have velocities that approach  $\sim 100$ -150 km/s. Common to all implosions on this platform, these objects may be tips of fingers or chunks of ablator, developed from instability growth, piercing and cooling the hotspot. A schematic of the orientation of the fill tube to both the equatorial and polar image frames is shown. Often at least one object appears correlated to the fill tube orientation, implying that a jet seeded by the fill tube is injecting brightly radiating CH into the hotspot [42]. The exact origin, the performance impact, and the role of these features in bringing mix into the hotspot are still under investigation.

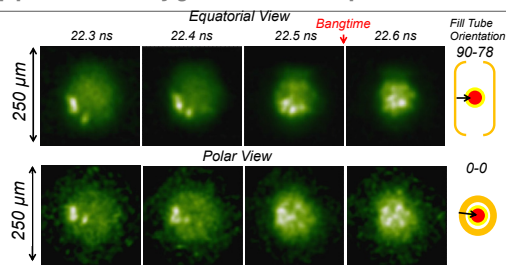


**Figure 21:** Time gated self-emission x-ray images of N130315 from an equatorial view obtained with the hGXD instrument, and the polar view (viewing into laser entrance hole) obtained from the GXD instrument. These frames show the evolution of the hot-spot shape around bangtime. Several bright spots of radiating plastic chunk are observed traversing the core near bangtime. These bright spot features are common to implosions in this campaign, partly due to the fact that the tritium fill radiates less than traditional  $D^3He$  Symcaps, accentuating higher  $Z$  emission from hot shell material.

## V. Summary and future work

A platform to study fuel and shell atomic scale mix at the NIF has been developed using tritium-filled CD Symcap implosions. Deuterium mixing into the implosion creates an unambiguous signature of atomic scale mix by producing DT fusion neutrons with the hot tritium core. By taking advantage of the advanced NIF diagnostic suite, this platform measures the TT and DT neutron simultaneously, ion temperature, X-ray and neutron core imaging, along with X-ray and nuclear bangtimes. The simultaneous measure of TT and DT neutrons places strong constraints on simulations by obtaining both core performance and atomic gas/shell mix, independently. CD layers flush with the gas/shell interface and recessed to up to 8  $\mu\text{m}$  have shown that most of the mix occurs at the inner shell surface. Ablation front instabilities may also play a role in the observed data and will be the topic of future efforts in simulation and experiments.

With a powerful new diagnostic mix platform now commissioned, experiments are being proposed to study a wide variety of topics. For example, increasing the implosion convergence closer to that of cryogenic DT experiments is now underway. The expectation is that this will further stress hydrodynamic

simulations and atomic-mix models, providing the opportunity for additional model development, while also being more relevant to ignition experiments. Experiments to combine X-ray tracer measurements in Ge and Cu doped capsules with CD layer are now being designed. One such design would include a CD layer with mostly hydrogen fill and trace tritium along with Cu and Ge “tri-doping.” This would provide simulations and redundant measurements of chunk mix from DD neutron and Cu and Ge emission (Cu and Ge placed at different ablator locations) with atomic-mix data from DT neutrons. Also experiments to quantify the seeds and role of ablation front instabilities in injected shell material in the hotspot are being proposed. One experimental concept is to simply repeat the 8  $\mu\text{m}$  recessed shot N130614 so that inner 8  $\mu\text{m}$  of the shell is CH but with the CD extending all the way from 8  $\mu\text{m}$  recessed through the thickness of the shell (instead of 4  $\mu\text{m}$  thick). If significant material is injected into the core via ablation front growth, the DT yield will be correspondingly higher than N130614. Finally, developing benchmarked mix models capable of designing targets robust to the deleterious performance losses due to mix is the ultimate goal of this campaign.

This work was performed under the auspices of the U.S. Department of Energy by Lawrence Livermore National Laboratory under Contract DE-AC52-07NA27344.

## VI. References

1. E. I. Moses, *Journal of Physics: Conference Series* **112** (1), 012003 (2008).
2. S. W. Haan, J. D. Lindl, D. A. Callahan, D. S. Clark, J. D. Salmonson, B. A. Hammel, L. J. Atherton, R. C. Cook, M. J. Edwards, S. Glenzer, A. V. Hamza, S. P. Hatchett, M. C. Herrmann, D. E. Hinkel, D. D. Ho, H. Huang, O. S. Jones, J. Kline, G. Kyrala, O. L. Landen, B. J. MacGowan, M. M. Marinak, D. D. Meyerhofer, J. L. Milovich, K. A. Moreno, E. I. Moses, D. H. Munro, A. Nikroo, R. E. Olson, K. Peterson, S. M. Pollaine, J. E. Ralph, H. F. Robey, B. K. Spears, P. T. Springer, L. J. Suter, C. A. Thomas, R. P. Town, R. Vesey, S. V. Weber, H. L. Wilkens and D. C. Wilson, *Physics of Plasmas* **18** (5), 051001 (2011).
3. J. Lindl, et al., *Physics of Plasmas* **11**, 339 (2004).
4. S. H. Glenzer, D. A. Callahan, A. J. MacKinnon, J. L. Kline, G. Grim, E. T. Alger, R. L. Berger, L. A. Bernstein, R. Betti, D. L. Bleuel, T. R. Boehly, D. K. Bradley, S. C. Burkhart, R. Burr, J. A. Caggiano, C. Castro, D. T. Casey, C. Choate, D. S. Clark, P. Celliers, C. J. Cerjan, G. W. Collins, E. L. Dewald, P. DiNicola, J. M. DiNicola, L. Divol, S. Dixit, T. Doeppner, R. Dylla-Spears, E. Dzenitis, M. Eckart, G. Erbert, D. Farley, J. Fair, D. Fittinghoff, M. Frank, L. J. A. Frenje, S. Friedrich, M. G. Johnson, C. Gibson, E. Giraldez, V. Glebov, S. Glenn, N. Guler, S. W. Haan, B. J. Haid, B. A. Hammel, A. V. Hamza, C. A. Haynam, G. M. Heestand, M. Hermann, H. W. Hermann, D. G. Hicks, D. E. Hinkel, J. P. Holder, D. M. Holunda, J. B. Horner, W. W. Hsing, H. Huang, N. Izumi, M. Jackson, O. S. Jones, D. H. Kalantar, R. Kauffman, J. D. Kilkenny, R. K. Kirkwood, J. Klingmann, T. Kohut, J. P. Knauer, J. A. Koch, B. Koziolowski, G. A. Kyrala, A. L. Kritcher, J. Kroll, K. L. Fortune, L. Lagin, O. L. Landen, D. W. Larson, D. LaTray, R. J. Leeper, S. L. Pape, J. D. Lindl, R. Lowe-Webb, T. Ma, J. McNaney, A. G. MacPhee, T. N. Malsbury, E. Mapoles, C. D. Marshall, N. B. Meezan, F. Merrill, P. Michel, J. D. Moody, A. S. Moore, M. Moran, K. A. Moreno, D. H. Munro, B. R. Nathan, A. Nikroo, R. E. Olson, C. D. Orth, A. E. Pak, P. K. Patel, T. Parham, R. Petrasso, J. E. Ralph, H. Rinderknecht, S. P. Regan, H. F. Robey, J. S. Ross, M. D. Rosen, R. Sacks, J. D. Salmonson, R. Saunders, J. Sater, C. Sangster, M. B. Schneider, F. H. Seguin, M. J. Shaw, B. K. Spears, P. T. Springer, W. Stoeffl, L. J. Suter, C. A. Thomas, R. Tommasini, R. P. J. Town, C. Walters, S. Weaver, S. V. Weber, P. J. Wegner, P. K. Whitman, K. Widmann, C. C. Widmayer, C. H. Wilde, D. C. Wilson, B. V. Wonterghem, B. J. MacGowan, L. J. Atherton, M. J. Edwards and E. I. Moses, *Physics of Plasmas* **19** (5), 056318 (2012).
5. S. P. Regan, R. Epstein, B. A. Hammel, L. J. Suter, J. Ralph, H. Scott, M. A. Barrios, D. K. Bradley, D. A. Callahan, C. Cerjan, G. W. Collins, S. N. Dixit, T. Doeppner, M. J. Edwards, D. R. Farley, S. Glenn, S. H. Glenzer, I. E. Golovkin, S. W. Haan, A. Hamza, D. G. Hicks, N. Izumi, J. D. Kilkenny, J. L. Kline, G. A. Kyrala, O. L. Landen, T. Ma, J. J. MacFarlane, R. C. Mancini, R. L. McCrory, N. B. Meezan, D. D. Meyerhofer, A. Nikroo, K. J. Peterson, T. C. Sangster, P. Springer and R. P. J. Town, *Physics of Plasmas* **19** (5), 056307 (2012).
6. T. Ma, et al., submitted to *Physical Review Letters*.
7. V. Smalyuk, et al., submitted to *Physical Review Letters*.
8. O. L. Landen, T. R. Boehly, D. K. Bradley, D. G. Braun, D. A. Callahan, P. M. Celliers, G. W. Collins, E. L. Dewald, L. Divol, S. H. Glenzer, A. Hamza, D. G.

- Hicks, N. Hoffman, N. Izumi, O. S. Jones, R. K. Kirkwood, G. A. Kyrala, P. Michel, J. Milovich, D. H. Munro, A. Nikroo, R. E. Olson, H. F. Robey, B. K. Spears, C. A. Thomas, S. V. Weber, D. C. Wilson, M. M. Marinak, L. J. Suter, B. A. Hammel, D. D. Meyerhofer, J. Atherton, J. Edwards, S. W. Haan, J. D. Lindl, B. J. MacGowan and E. I. Moses, *Physics of Plasmas* **17** (5), 056301-056308 (2010).
9. D. C. Wilson, P. S. Ebey, T. C. Sangster, W. T. Shmayda, V. Y. Glebov and R. A. Lerche, *Physics of Plasmas* **18** (11), 112707 (2011).
10. J. R. Rygg, J. A. Frenje, C. K. Li, F. H. Séguin, R. D. Petrasso, J. A. Delettrez, V. Y. Glebov, V. N. Goncharov, D. D. Meyerhofer, P. B. Radha, S. P. Regan and T. C. Sangster, *Physics of Plasmas* **14** (5), 056306 (2007).
11. J. R. Rygg, J. A. Frenje, C. K. Li, F. H. Séguin, R. D. Petrasso, V. Y. Glebov, D. D. Meyerhofer, T. C. Sangster and C. Stoeckl, *Physical Review Letters* **98** (21), 215002 (2007).
12. T. R. Boehly, D. L. Brown, R. S. Craxton, R. L. Keck, J. P. Knauer, J. H. Kelly, T. J. Kessler, S. A. Kumpan, S. J. Loucks, S. A. Letzring, F. J. Marshall, R. L. McCrory, S. F. B. Morse, W. Seka, J. M. Soures and C. P. Verdon, *Optics Communications* **133** (1-6), 495-506 (1997).
13. J. D. Moody, P. Michel, L. Divol, R. L. Berger, E. Bond, D. K. Bradley, D. A. Callahan, E. L. Dewald, S. Dixit, M. J. Edwards, S. Glenn, A. Hamza, C. Haynam, D. E. Hinkel, N. Izumi, O. Jones, J. D. Kilkenny, R. K. Kirkwood, J. L. Kline, W. L. Kruer, G. A. Kyrala, O. L. Landen, S. LePape, J. D. Lindl, B. J. MacGowan, N. B. Meezan, A. Nikroo, M. D. Rosen, M. B. Schneider, D. J. Strozzi, L. J. Suter, C. A. Thomas, R. P. J. Town, K. Widmann, E. A. Williams, L. J. Atherton, S. H. Glenzer and E. I. Moses, *Nat Phys* **8** (4), 344-349 (2012).
14. D. S. Clark, S. W. Haan, B. A. Hammel, J. D. Salmonson, D. A. Callahan and R. P. J. Town, *Physics of Plasmas* **17** (5), 052703 (2010).
15. R. E. Tipton (private communication).
16. G. Dimonte and R. Tipton, *Physics of Fluids* **18** (8), 085101 (2006).
17. J. Pino, to be published.
18. D. S. Clark, S. W. Haan, A. W. Cook, M. J. Edwards, B. A. Hammel, J. M. Koning and M. M. Marinak, *Physics of Plasmas* **18** (8), 082701 (2011).
19. S. Atzeni and J. Meyer-ter-Vehn, *The physics of inertial fusion*. (Oxford University Press, Oxford, 2004).
20. R. J. Slobodrian, *Reports on Progress in Physics* **34** (1), 175 (1971).
21. I. J. Thompson and S. Quaglioni (private communication).
22. C. Wong, J. D. Anderson and J. W. McClure, *Nuclear Physics* **71** (1), 106-112 (1965).
23. K. W. Allen, E. Almqvist, J. T. Dewan, T. P. Pepper and J. H. Sanders, *Phys Rev* **82** (2), 262 (1951).
24. S. J. Bame and W. T. Leland, *Phys Rev* **106** (6), 1257 (1957).
25. D. T. Casey, J. A. Frenje, M. Gatu Johnson, M. J. E. Manuel, N. Sinenian, A. B. Zylstra, F. H. Séguin, C. K. Li, R. D. Petrasso, V. Y. Glebov, P. B. Radha, D. D. Meyerhofer, T. C. Sangster, D. P. McNabb, P. A. Amendt, R. N. Boyd, S. P. Hatchett, S. Quaglioni, J. R. Rygg, I. J. Thompson, A. D. Bacher, H. W. Herrmann and Y. H. Kim, *Physical Review Letters* **109** (2), 025003 (2012).
26. D. B. Sayre, Submitted to *Physical Review Letters* (2013).
27. C. B. Yeamans, D. L. Bleuel and L. A. Bernstein, *Review of Scientific Instruments* **83** (10), 10D315 (2012).
28. R. A. Lerche, V. Y. Glebov, M. J. Moran, J. M. McNaney, J. D. Kilkenny, M. J. Eckart, R. A. Zacharias, J. J. Haslam, T. J. Clancy, M. F. Yeoman, D. P. Warwas,

- T. C. Sangster, C. Stoeckl, J. P. Knauer and C. J. Horsfield, Review of Scientific Instruments **81** (10), 10D319 (2010).
29. V. Y. Glebov, T. C. Sangster, C. Stoeckl, J. P. Knauer, W. Theobald, K. L. Marshall, M. J. Shoup, Iii, T. Buczek, M. Cruz, T. Duffy, M. Romanofsky, M. Fox, A. Pruyne, M. J. Moran, R. A. Lerche, J. McNaney, J. D. Kilkenny, M. J. Eckart, D. Schneider, D. Munro, W. Stoeffl, R. Zacharias, J. J. Haslam, T. Clancy, M. Yeoman, D. Warwas, C. J. Horsfield, J. L. Bourgade, O. Landoas, L. Disdier, G. A. Chandler and R. J. Leeper, Review of Scientific Instruments **81** (10), 10D325-326 (2010).
  30. M. G. Johnson, J. A. Frenje, D. T. Casey, C. K. Li, F. H. Seguin, R. Petrasso, R. Ashabranner, R. M. Bionta, D. L. Bleuel, E. J. Bond, J. A. Caggiano, A. Carpenter, C. J. Cerjan, T. J. Clancy, T. Doeppner, M. J. Eckart, M. J. Edwards, S. Friedrich, S. H. Glenzer, S. W. Haan, E. P. Hartouni, R. Hatarik, S. P. Hatchett, O. S. Jones, G. Kyrala, S. L. Pape, R. A. Lerche, O. L. Landen, T. Ma, A. J. MacKinnon, M. A. McKernan, M. J. Moran, E. Moses, D. H. Munro, J. McNaney, H. S. Park, J. Ralph, B. Remington, J. R. Rygg, S. M. Sepke, V. Smalyuk, B. Spears, P. T. Springer, C. B. Yeamans, M. Farrell, D. Jasion, J. D. Kilkenny, A. Nikroo, R. Paguio, J. P. Knauer, V. Y. Glebov, T. C. Sangster, R. Betti, C. Stoeckl, J. Magoon, M. J. Shoup, III, G. P. Grim, J. Kline, G. L. Morgan, T. J. Murphy, R. J. Leeper, C. L. Ruiz, G. W. Cooper and A. J. Nelson, Review of Scientific Instruments **83** (10), 10D308 (2012).
  31. D. T. Casey, J. A. Frenje, M. G. Johnson, F. H. Seguin, C. K. Li, R. D. Petrasso, V. Y. Glebov, J. Katz, J. Magoon, D. D. Meyerhofer, T. C. Sangster, M. Shoup, J. Ulreich, R. C. Ashabranner, R. M. Bionta, A. C. Carpenter, B. Felker, H. Y. Khater, S. LePape, A. MacKinnon, M. A. McKernan, M. Moran, J. R. Rygg, M. F. Yeoman, R. Zacharias, R. J. Leeper, K. Fletcher, M. Farrell, D. Jasion, J. Kilkenny and R. Paguio, Review of Scientific Instruments **84** (4), 043506 (2013).
  32. J. A. Frenje, R. Bionta, E. J. Bond, J. A. Caggiano, D. T. Casey, C. Cerjan, J. Edwards, M. Eckart, D. N. Fittinghoff, S. Friedrich, V. Y. Glebov, S. Glenzer, G. Grim, S. Haan, R. Hatarik, S. Hatchett, M. G. Johnson, O. S. Jones, J. D. Kilkenny, J. P. Knauer, O. Landen, R. Leeper, S. L. Pape, R. Lerche, C. K. Li, A. MacKinnon, J. McNaney, F. E. Merrill, M. Moran, D. H. Munro, T. J. Murphy, R. D. Petrasso, R. Rygg, T. C. Sangster, F. H. Séguin, S. Sepke, B. Spears, P. Springer, C. Stoeckl and D. C. Wilson, Nuclear Fusion **53** (4), 043014 (2013).
  33. J. Caggiano et al., to be published.
  34. B. K. Spears, S. Glenzer, M. J. Edwards, S. Brandon, D. Clark, R. Town, C. Cerjan, R. Dylla-Spears, E. Mapoles, D. Munro, J. Salmonson, S. Sepke, S. Weber, S. Hatchett, S. Haan, P. Springer, E. Moses, J. Kline, G. Kyrala and D. Wilson, Physics of Plasmas **19** (5), 056316 (2012).
  35. A. J. MacKinnon, J. L. Kline, S. N. Dixit, S. H. Glenzer, M. J. Edwards, D. A. Callahan, N. B. Meezan, S. W. Haan, J. D. Kilkenny, T. Döppner, D. R. Farley, J. D. Moody, J. E. Ralph, B. J. MacGowan, O. L. Landen, H. F. Robey, T. R. Boehly, P. M. Celliers, J. H. Eggert, K. Krauter, G. Frieders, G. F. Ross, D. G. Hicks, R. E. Olson, S. V. Weber, B. K. Spears, J. D. Salmonsens, P. Michel, L. Divol, B. Hammel, C. A. Thomas, D. S. Clark, O. S. Jones, P. T. Springer, C. J. Cerjan, G. W. Collins, V. Y. Glebov, J. P. Knauer, C. Sangster, C. Stoeckl, P. McKenty, J. M. McNaney, R. J. Leeper, C. L. Ruiz, G. W. Cooper, A. G. Nelson, G. G. A. Chandler, K. D. Hahn, M. J. Moran, M. B. Schneider, N. E. Palmer, R. M. Bionta, E. P. Hartouni, S. LePape, P. K. Patel, N.

- Izumi, R. Tommasini, E. J. Bond, J. A. Caggiano, R. Hatarik, G. P. Grim, F. E. Merrill, D. N. Fittinghoff, N. Guler, O. Drury, D. C. Wilson, H. W. Herrmann, W. Stoeffl, D. T. Casey, M. G. Johnson, J. A. Frenje, R. D. Petrasso, A. Zylestra, H. Rinderknecht, D. H. Kalantar, J. M. Dzenitis, P. Di Nicola, D. C. Eder, W. H. Courdin, G. Gururangan, S. C. Burkhardt, S. Friedrich, D. L. Blueuel, I. A. Bernstein, M. J. Eckart, D. H. Munro, S. P. Hatchett, A. G. Macphee, D. H. Edgell, D. K. Bradley, P. M. Bell, S. M. Glenn, N. Simanovskaia, M. A. Barrios, R. Benedetti, G. A. Kyrala, R. P. J. Town, E. L. Dewald, J. L. Milovich, K. Widmann, A. S. Moore, G. LaCaille, S. P. Regan, L. J. Suter, B. Felker, R. C. Ashabraner, M. C. Jackson, R. Prasad, M. J. Richardson, T. R. Kohut, P. S. Datte, G. W. Krauter, J. J. Klingman, R. F. Burr, T. A. Land, M. R. Hermann, D. A. Latray, R. L. Saunders, S. Weaver, S. J. Cohen, L. Berzins, S. G. Brass, E. S. Palma, R. R. Lowe-Webb, G. N. McHalle, P. A. Arnold, L. J. Lakin, C. D. Marshall, G. K. Brunton, D. G. Mathisen, R. D. Wood, J. R. Cox, R. B. Ehrlich, K. M. Knittel, M. W. Bowers, R. A. Zacharias, B. K. Young, J. P. Holder, J. R. Kimbrough, T. Ma, K. N. La Fortune, C. C. Widmayer, M. J. Shaw, G. V. Erbert, K. S. Jancaitis, J. M. DiNicola, C. Orth, G. Heestand, R. Kirkwood, C. Haynam, P. J. Wegner, P. K. Whitman, A. Hamza, E. G. Dzenitis, R. J. Wallace, S. D. Bhandarkar, T. G. Parham, R. Dylla-Spears, E. R. Mapoles, B. J. Kozioziemski, J. D. Sater, C. F. Walters, B. J. Haid, J. Fair, A. Nikroo, E. Giraldez, K. Moreno, B. Vanwonterghem, R. L. Kauffman, S. Batha, D. W. Larson, R. J. Fortner, D. H. Schneider, J. D. Lindl, R. W. Patterson, L. J. Atherton and E. I. Moses, *Physical Review Letters* **108** (21), 215005 (2012).
36. G. Grim, to be published.
37. P. M. Bell, D. K. Bradley, J. D. Kilkenny, A. Conder, C. Cerjan, C. Hagmann, D. Hey, N. Izumi, J. Moody, A. Teruya, J. Celeste, J. Kimbrough, H. Khater, M. J. Eckart and J. Ayers, *Review of Scientific Instruments* **81** (10), 10E540 (2010).
38. S. M. Glenn, L. R. Benedetti, D. K. Bradley, B. A. Hammel, N. Izumi, S. F. Khan, G. A. Kyrala, T. Ma, J. L. Milovich, A. E. Pak, V. A. Smalyuk, R. Tommasini and R. P. Town, *Review of Scientific Instruments* **83** (10), 10E519 (2012).
39. D. H. Edgell, D. K. Bradley, E. J. Bond, S. Burns, D. A. Callahan, J. Celeste, M. J. Eckart, V. Y. Glebov, D. S. Hey, G. Lacaille, J. D. Kilkenny, J. Kimbrough, A. J. Mackinnon, J. Magoon, J. Parker, T. C. Sangster, M. J. Shoup, III, C. Stoeckl, T. Thomas and A. MacPhee, *Review of Scientific Instruments* **83** (10), 10E119 (2012).
40. S. F. Khan, P. M. Bell, D. K. Bradley, S. R. Burns, J. R. Celeste, L. S. Dauffy, M. J. Eckart, M. A. Gerhard, C. Hagmann, D. I. Headley, J. P. Holder, N. Izumi, M. C. Jones, J. W. Kellogg, H. Y. Khater, J. R. Kimbrough, A. G. Macphee, Y. P. Opachich, N. E. Palmer, R. B. Petre, J. L. Porter, R. T. Shelton, T. L. Thomas and J. B. Worden, 850505-850505 (2012).
41. H. G. Rinderknecht, M. G. Johnson, A. B. Zylstra, N. Sinenian, M. J. Rosenberg, J. A. Frenje, C. J. Waugh, C. K. Li, F. H. Seguin, R. D. Petrasso, J. R. Rygg, J. R. Kimbrough, A. MacPhee, G. W. Collins, D. Hicks, A. Mackinnon, P. Bell, R. Bionta, T. Clancy, R. Zacharias, T. Doppner, H. S. Park, S. LePape, O. Landen, N. Meezan, E. I. Moses, V. U. Glebov, C. Stoeckl, T. C. Sangster, R. Olson, J. Kline and J. Kilkenny, *Review of Scientific Instruments* **83** (10), 10D902 (2012).
42. S. H. Langer, N. Izumi, T. R. Dittrich and S. W. Haan, *High Energy Density Physics* **3** (1–2), 169-174 (2007).

# Indirect Drive Exploding Pusher on the NIF

S. Le Pape,<sup>1</sup> L. Divol,<sup>1</sup> L. Berzak Hopkins,<sup>1</sup> A. Mackinnon,<sup>1</sup> N. Meezan,<sup>1</sup> J. Frenje,<sup>2</sup> H. Herrmann,<sup>3</sup> J. McNaney,<sup>1</sup> G. Grim,<sup>3</sup> J. Knauer,<sup>4</sup> R. Petrasso,<sup>2</sup> A. Zylstra,<sup>2</sup> H. Rinderknecht,<sup>2</sup> and J. D. Kilkenny<sup>5</sup>

<sup>1</sup> Lawrence Livermore National Laboratory, Livermore, CA 94550

<sup>2</sup> Plasma Science and Fusion Center, Massachusetts Institute of Technology, Cambridge, Massachusetts 02139

<sup>3</sup> Los Alamos National Laboratory, Los Alamos, New Mexico 87545

<sup>4</sup> Laboratory for Laser Energetics, University of Rochester, 250 E. River Road, Rochester, NY 14623

<sup>5</sup> General Atomics Corporation, La Jolla, CA

The first two Indirect Drive Exploding Pusher (IDEP) experiments have been carried out on the National Ignition Facility laser system. This new platform was designed to provide a high yield neutron source for nuclear diagnostic calibration. The IDEP platform is designed to generate a high yield of deuterium and tritium (DT) neutrons ( $> 210^{14}$ ) in an implosion with very low  $\rho r < 30 \text{ mg/cm}^2$  and low bulk motion velocity ( $< 30 \text{ km/s}$ ). The IDEP platform will be used to calibrate the Nuclear Activation Diagnostics (NADs) and to measure the scattering contribution of the hohlraum thermo-mechanical package and other scattering sources using the neutron Time-of-Flight detectors (nToF) and Magnetic Recoil Spectrometer (MRS). In addition, the IDEP platform provides an opportunity to study ICF physics in a system much simpler than typical gas-filled symmetry capsule (symcap) or DT-layered implosions.

The neutron yield measured on the first experiments is in close agreement with the 1D yield predicted by the HYDRA simulation. HYDRA simulations were done with the high-flux DCA model [1] without requiring multipliers usually applied to the X-ray drive to match the implosion velocity [2]. When the capsule gas mixture was changed from pure deuterium gas (DD) to a 50/50 DT mixture, the neutron yield increased by a predicted factor of approximately 100, scaling with

the nuclear cross section. The experiments use a cryogenic “near vacuum” hohlraum at a temperature of 32 K. The hohlraum are Au, 30 microns thick, 9.44 cm in length with a diameter of 5.44 mm and are filled with helium at a density of  $0.32 \text{ mg/cm}^3$ , approximately 1/30 of the typical density of NIF gas-filled hohlraum. The hohlraum is heated by 192 frequency-tripled laser beams at a wavelength of 351 nm through two laser entrance holes (LEHs) of 3.1 mm diameter at either end. The beams are arranged in two cones entering through each LEH, the inner cone at angles of 23.5 and 30 degree and the outer cone at 44.5 and 50 degree to the vertical axis.

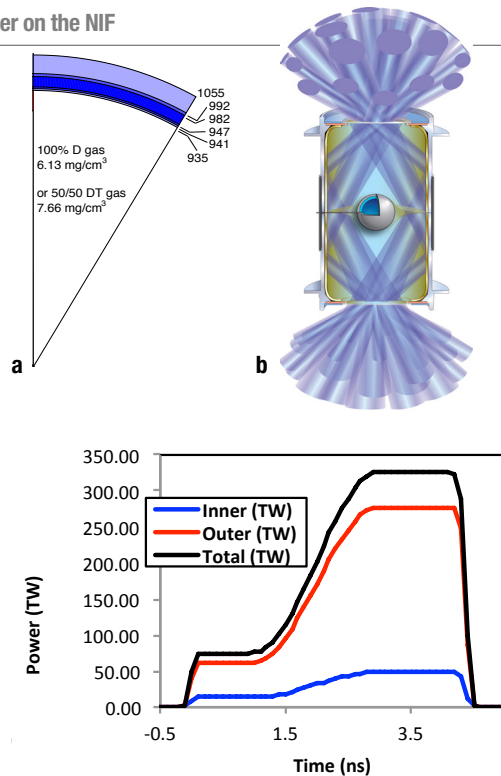


**Figure 22:** (a): Pie diagram of the capsule; (b): NIF hohlraum and beam distribution in the hohlraum; and (c): laser pulse shape.

In high convergence, high pr experiments on the NIF, the symmetry of the compressed core is tuned through the crossbeam energy transfer process [3] between inner and outer beams induced by the wavelength separation between the cones. Due to the hot, low-density plasma inside the IDEP hohlraum, crossbeam energy transfer is predicted to be negligible when the wavelength difference between the inner and outer cones is set to zero. The symmetry of the core is tuned using the energy repartition between the inner and outer beams (cone fraction) rather than the

crossbeam energy transfer process. The cone fraction to achieve a symmetrical implosion was set to 0.15. The laser pulse is 4.3 ns long with a peak power of 325 TW and total energy of 933 kJ. To limit hydro coupling [4] induced both by the gold expanding from the walls and the CH expanding from the LEH windows, a 2.0 ns 75 TW foot on the laser pulse is introduced in order to ablate enough CH from the capsule to protect the fuel and limit the gold and window expansion

The x-ray drive is incident on a spherical capsule with an outer radius of  $1055 \mu\text{m} \pm 15 \mu\text{m}$ , and with a  $120 \mu\text{m} \pm 5 \mu\text{m}$  thick ablator, consisting of multilayered plastic (CH) with a graded silicon dopant. The capsule is filled with DD or DT gas. The capsule absorbs x-rays from the hohlraum for several ns before burning through, when the radiation front completely penetrates the ablator. The exploding ablator launches a single strong shock into the gas fuel that stagnates at the center, generating nuclear yield. Target capsules are Graded Doped Plastic silicon dopant and are filled either with pure deuterium gas at a density of  $6.33 \text{ mg/cm}^3$  or deuterium-tritium gas at  $7.66 \text{ mg/cm}^3$ , maintaining number density between the gas fill

The performance of these targets was diagnosed using a suite of x-ray and nuclear diagnostics [5]. Overall the experimental measurements are very close to HYDRA calculations with undegraded drive.



	N130313	HYDRA Postshot		N130503	HYDRA Postshot
DD neutron yield	5.1 e12	4.3e12	DT neutron yield	5.13e14	4.37e14
DD Tion (keV)	3.5	3.53	DT neutron temp (keV)	4.62	4.64
X ray bang time (ns)	4.82	4.74	DD neutron yield	1.54e12	1.72e12
MO ( $\mu\text{m}$ )	197.34	200.5	DD Tion (keV)	4.2	4.02
Figure of Merit	0.5%	0.6%	X ray bang time (ns)	4.9	4.72
Peak radiation temperature (eV)	293	290	Neutron bang time (ns)	4.64	4.46
Fuel $\rho\text{R}$	14-18 mg/cm <sup>2</sup>	15.5 $\pm$ 1.6 mg/cm <sup>2</sup>	PO ( $\mu\text{m}$ )	219	216
Ablator $\rho\text{R}$	45-60 mg/cm <sup>2</sup>	44 $\pm$ 7 mg/cm <sup>2</sup>	DSR	0.24%	0.086%
Second DD-DT ratio	0.13%	0.18%	Peak radiation temperature (eV)	293	294

**Table 3** Summary of the performance of the DD shot (N131203) and the DT shot (N130503) compared to the corresponding post-shot hydra simulations

The coupling from laser light to hohlraum was measured to be 99%, which is consistent with previous experiments on the NIF [1] that have shown that the level of backscattered light due to laser instabilities in vacuum hohlraum was less than 2 percent leading to high laser to hohlraum coupling. The x-ray drive delivered by this pulse gave a peak radiation temperature measured by DANTE [6] of 293 eV  $\pm$  5 eV. As shown on Table 3, the experimental x-ray drive as a function of time (black curve) is accurately described by the HYDRA DCA high-flux model (red curve) [2], while HYDRA XSN models are approximately 8 eV too low. As a result of the drive agreement, the x-ray bang time measured by south pole bang time [7] and the predicted x-ray bang time are within 80 ps.

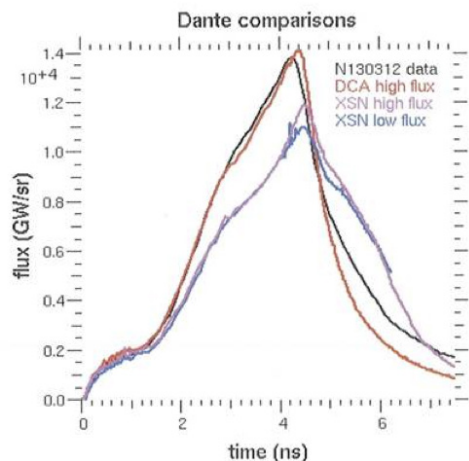


**Figure 23:** Measured radiative temperature as a function of time (black curve). Post-shot simulation of the radiation temperature with various atomic models.

DCA high flux (red curve), XSN high flux (pink curve), XSN low flux (blue curve)

In a high-convergence ICF implosion, the shock wave reflected from the center would propagate back through the fuel and reflect again off of the dense, imploding ablator, thus beginning the compression phase of the implosion and leading to a rapid succession of reflected waves that quasi-isentropically compress the fuel. In the IDEP, however, the reflected wave encounters only a low-density ablator at large radius (200  $\mu\text{m}$ ). Very little compression occurs after the initial shock, so the nuclear yield is generated in a symmetric, low hr. system. If we define the convergence ratio of the fuel (CR) as the initial ablator inner radius divided by the hot-spot radius at bang-time, the IDEP reaches  $\text{CR} \leq 5$ . This design also has the added benefit of generating most of its yield below the “fall-line” the fastest trajectory of ablator material in the implosion. Thus, the nuclear performance is expected to be robust to fuel/ablator mix. To achieve low  $\rho\text{r}$ , the capsule only converges by about a factor of 5 from its initial radius, when high  $\rho\text{r}$ /convergence target are usually converging by a factor of 30. To limit the convergence of the shell to 5 x and achieve a yield above  $10^{14}$  neutron, the density of the DT gas fill was set to 7.66 mg/cm<sup>3</sup> (6.33 mg/cm<sup>3</sup>). The hot spot symmetry (Figure 23) is determined using a gated x-ray imager above 4 keV [8]. The implosion x-ray image was

very round with mode  $M=2-4$  below 0.5% and a hot spot radius  $M0=200\mu\text{m}$ . Because of the low convergence, (the large  $M0$ ), the x-ray image shows both the self-emission of the hot gas (DD or DT) at the center of the image and the emission of the hotter CH of the shell, i.e., limb brightening.

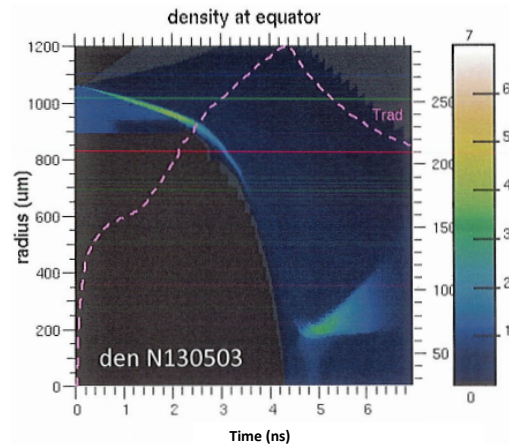


**Figure 24:** Radiation temperature superimposed on the equatorial density evolution as a function of time

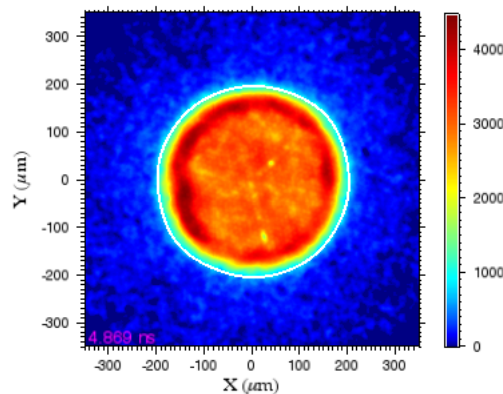


**Figure 25:** Polar view of the implosion self-emission at bang time for IDEP N130312-001-999. Azymutal symmetry is excellent with mode  $M=2-4$  below 0.5%

The neutron burn history (see Figure 28), recorded by the gamma ray history detector [9], shows a sharp rising front on the neutron yield with a long tail of approximately 400ps. The sharp rise is associated with the neutron yield generated at shock flash, and the long tail is generated as the shock wave propagates outward after shock flash. As predicted by the HYDRA simulation, the shape of the neutron burn history confirms that the shock flash

produces most of the yield and almost none of the yield is produced by compression of the hot spot.

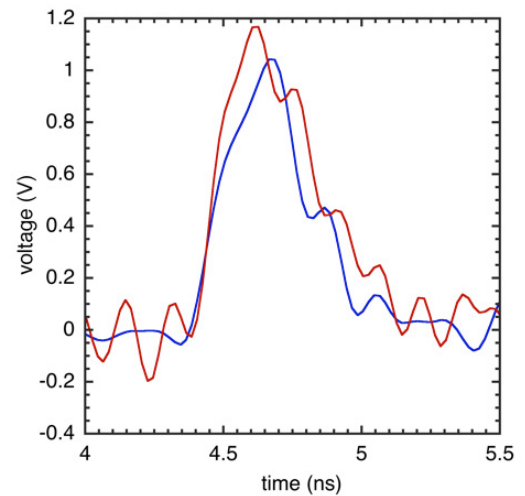


**Figure 26:** Neutron burn history recorded by the gamma ray history detector at two energies 10 MeV (red curve), 8 MeV (blue curve), and simulated burn history (black curve).

The  $\rho r$  of the implosion is measured independently by three different diagnostics depending on capsule gas fill. On the pure DD shot, the background D ions fuse in-flight with  $^3\text{He}$  ions generated by the D-D reaction, generating 14.7 MeV protons via the reaction path  $\Delta + 3\text{H} \rightarrow \pi + \alpha$ . The slowing down of these protons provides an independent measure of the total  $\rho r$  in the system. The proton spectrum is recorded by the wedge range filter (WRF) [10] on both polar and equatorial axes. In addition, the fuel  $\rho r$  can also be inferred from the ratio of the secondary DT neutrons to the primary DD yield, as measured by the neutron Time-of-Flight detectors (nToF) [11]. This data indicate a total  $\rho r = 44 \pm 7 \text{ mg/cm}^2$ , similar to the 45 to 60  $\text{mg/cm}^2$  range predicted by HYDRA simulations. For the DT capsule fill, the downscattered ratio (DSR) of the 14.7 MeV neutrons is defined as the number of neutrons detected with energies between 10 to 12 MeV divided by the number of primary neutrons in the 13 to 15 MeV energy range. The DSR is proportional to the total  $\rho r$ , which is independently measured by secondary particle diagnostics. The spatially average DSR for the implosion is obtained using the magnetic

recoil spectrometer (MRS) [12] and three high dynamic range NTOFS [11]. They measure Down Scatter Ratio (DSR) as 0.25% above the noise floor, similar to the 0.01% predicted by the HYDRA simulation. These data also indicate that the implosion easily meets the design goal of  $pr < 130\text{mg/cm}^2$ .

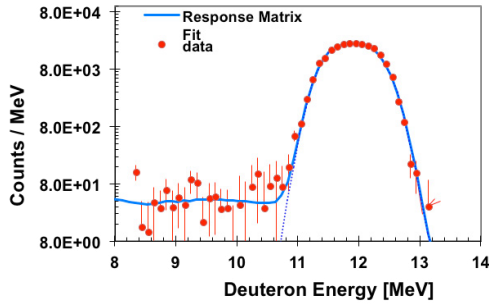


**Figure 27:** DT neutron spectrum measured with the magnetic recoil spectrometer

Because the neutron yield recorded by the activation foils is sensitive to the apparent ion temperature at the position of the detector, an additional design goal of the IDEP platform was to produce a low-bulk velocity neutron source for the calibration of the various flange NADs [13] located around the chamber. The bulk velocity of the IDEP implosion is measured by three different nToF's on different lines of sight and is measured to be less than 20 km/s on all three axes. This measurement was confirmed by the neutron yield measurement from 19 different flange NADs [13] located around the target chamber that exhibited a deviation from the flat field of less than 10%.

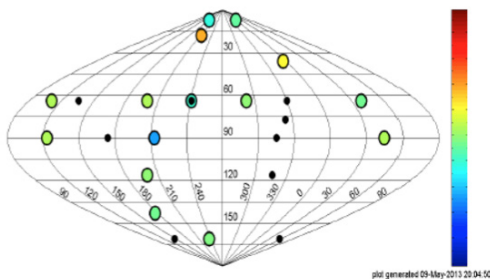


**Figure 28:** Yield variation around the target chamber measured by the Flange NADs

In summary, the NIF facility has begun commissioning a new platform, the Indirect Drive Exploding Pusher. The IDEP design has been validated with a two shots: a DD fuel shot N130312-001-999 and corresponding DT shot N130503-001-999 that provided calibration data for nuclear diagnostics such as the nToF's, MRS, and flange NADs. The IDEP also provides a simpler platform with which to study hohlraum physics and capsule implosion physics. The low-convergence implosion occurs in a near-vacuum hohlraum with very little (less than a percent) backscattered light and negligible crossbeam power transfer. This model was developed, in part, to improve agreement between simulations and vacuum hohlraum data from the 2009 hohlraum energetics campaign. The implosion consists of a single strong shock in the gas fuel with a negligible compression phase, resulting in a symmetric burn that appears to be free of hydrodynamic mix. Hohlraum performance is consistent with the DCA, high-flux hohlraum model in HYDRA.

We plan to utilize this platform by systematically modifying the hohlraum, capsule, and laser pulse. These modifications will allow careful observation of performance degradation as the hohlraum and implosion characteristics approach those of ignition experiments.

This work was performed under the auspices of the U.S. Department of Energy by Lawrence Livermore National Laboratory under Contract DE-AC52-07NA27344. Work was also supported by the Laboratory Directed Research and Development Grant 11-ERD-050 and the National Laboratory User Facility.

## I. REFERENCES

- [1] J. L. Kline, S. H. Glenzer, R. E. Olson, L. J. Suter, K. Widmann, D. A. Callahan, S. N. Dixit, C. A. Thomas, D. E. Hinkel, E. A. Williams, et al., *Physical Review Letters* **106**, 085003 (2011).
- [2] R. E. Olson, L. J. Suter, J. L. Kline, D. A. Callahan, M. D. Rosen, S. N. Dixit, O. L. Landen, N. B. Meezan, J. D. Moody, C. A. Thomas, et al., *Physics of Plasmas* **19**, 053301 (2012).
- [3] P. Michel, L. Divol, E. A. Williams, C. A. Thomas, D. A. Callahan, S. Weber, S. W. Haan, J. D. Salmonson, N. B. Meezan, O. L. Landen, et al., *Physics of Plasmas* **16**, 042702 (2009).
- [4] D. E. Hinkel, S. W. Haan, A. B. Langdon, T. R. Dittrich, C. H. Still, and M. M. Marinak, *Physics of Plasmas* **11**, 1128 (2004).
- [5] M. J. Edwards, J. D. Lindl, B. K. Spears, S. V. Weber, L. J. Atherton, D. L. Bleuel, D. K. Bradley, D. A. Callahan, C. J. Cerjan, D. Clark, et al., *Physics of Plasmas* **18**, 051003 (2011).
- [6] E. L. Dewald, K. M. Campbell, R. E. Turner, J. P. Holder, O. L. Landen, S. H. Glenzer, R. L. Kauffman, L. J. Suter, M. Landon, and M. Rhodes, *Review of Scientific Instruments* **75**, 3759 (2004).
- [7] D. Edgell, D. Bradley, E. J. Bond, S. Burns, D. Callahan, J. Celeste, M. J. Eckart, V. Y. Glebov, D. Hey, G. Lacaille, et al., *Review of Scientific Instruments* **83**, 10E119 (2012), ISSN 0034-6748.
- [8] J. Oertel, R. Aragonez, T. Archuleta, C. Barnes, L. Casper, V. Fatherley, T. Heinrichs, R. King, D. Landers, F. Lopez, et al., *Review of Scientific Instruments* **77**, 10E308 (2006), ISSN 0034-6748.
- [9] H. W. Herrmann, N. Hoffman, D. C. Wilson, W. Stoeffl, L. Dauffy, Y. H. Kim, A. McEvoy, C. S. Young, J. M. Mack, C. J. Horsfield, et al., *Review of Scientific Instruments* **81**, 10D333 (2010).
- [10] F. Seguin, N. Sinenian, M. Rosenberg, A. Zylstra, M. J. E. Manuel, H. Sio, C. Waugh, H. G. Rinderknecht, M. G. Johnson, J. Frenje, et al., *Review of Scientific Instruments* **83**, 10D908 (2012), ISSN 0034-6748.
- [11] V. Y. Glebov, D. D. Meyerhof, T. C. Sangster, C. Stoeckl, S. Roberts, C. A. Barrera, J. R. Celeste, C. J. Cerjan, L. S. Dauffy, D. C. Eder, et al., *Review of Scientific Instruments* **77**, 10E715 (2006).
- [12] J. Frenje, K. Green, D. Hicks, C. Li, F. S'eguín, R. Petrasso, T. Sangster, T. Phillips, V. Glebov, and D. Meyerhofer, *Review of Scientific Instruments* **72**, 854 (2001).
- [13] D. Bleuel, C. B. Yeaman, L. Bernstein, R. Bionta, J. A. Caggiano, D. T. Casey, G. Cooper, O. Drury, J. A. Frenje, C. Hagmann, et al., *Review of Scientific Instruments* **83**, 10D313 (2012), ISSN 0034-6748.

# Radiochemical determination of inertial confinement fusion capsule compression at the National Ignition Facility

D. A. Shaughnessy, K. J. Moody, P. M. Grant, N. Gharibyan, J. M. Gostic, P.T. Wooddy, P. C. Torretto, B. B. Bandong, C. J. Cerjan, C. A. Hagmann, J. A. Caggiano, L. A. Bernstein, D. H. Schneider, E. A. Henry, and R. J. Fortner

*Lawrence Livermore National Laboratory, 7000 East Avenue, Livermore, California 94550, USA*

## I. Introduction

The promise of safe, clean, inexhaustible energy has led to research in controlled fusion methods that could one day be integrated into commercial electrical power supplies. One of the paths toward laboratory scale fusion is inertial confinement fusion (ICF), in which a mixture of deuterium and tritium (DT) is compressed to extremely high densities and temperatures by high energy lasers [1, 2]. If sufficiently high density and temperature are achieved before the DT target disassembles, the fusion reactions between the two hydrogen isotopes produces alpha particles ( $^4\text{He}$ ) that can initiate a self-sustaining burn wave (ignition) in the fuel resulting in more energy being generated than is supplied by the initiating laser beams [3]. The conditions necessary for ignition and the energy gain factor (defined as the ratio of energy produced to the input laser energy) are both being explored at the National Ignition Facility (NIF), a large-scale, laser-driven, inertial-confinement-fusion complex constructed at the Lawrence Livermore National Laboratory (LLNL) [4].

Even in the absence of an ignition burn, heating and compressing the DT fuel can result in the production of a significant number of neutrons as well as alpha particles. The fraction of the thermonuclear fuel that undergoes nuclear reactions is roughly proportional to the product of its density and the time

during which compression is maintained (the confinement time). The confinement of the reacting fuel is of limited duration, determined by the inertia compressibility of the fuel mass. Fuel compressions to areal densities greater than  $1 \text{ g/cm}^2$  allow an alpha-driven burn wave to be achieved [5].

The Q-value of the  $^3\text{H}(^2\text{H},n)^4\text{He}$  reaction, which is by far the most probable reaction between hydrogen isotopes at the multi-keV ignition temperatures [6], is 17.6 MeV and results in the production of neutrons with a narrow energy distribution centered around 14.1 MeV. For a given amount of fuel in the spherical ICF capsule, increased compression results in higher areal density ( $\rho R$ ) and a corresponding increase in the probability for a neutron to scatter off the residual hydrogen isotopes before it leaves the fuel. Multiple scattering results in a substantial fraction of the neutrons that escape the fuel being downscattered to energies between 14 MeV and those associated with keV-thermal temperatures. The neutrons emitted by the imploded capsule (both 14.1 MeV and lower energy downscattered neutrons) can induce nuclear reactions, and therefore produce radionuclides, in material located in proximity to the capsule. The downscattered neutrons have fewer reaction pathways energetically available to them than the

14.1-MeV neutrons, with the lowest-energy fraction producing  $(n,\gamma)$  and  $(n,n')$  products. In contrast, the unscattered neutrons produce few capture products, preferentially forming products of threshold reactions, e.g.  $(n,2n)$  [7].

The ratio of the concentrations of  $(n,\gamma)$  to  $(n,2n)$  products produced in an activation target is related to the fraction of the emitted neutrons that have undergone multiple scattering and is, therefore, related to fuel compression. In the present paper, we report the observation of radioactive nuclei produced in gold targets exposed to the neutron fields generated from ICF capsules and demonstrate the potential diagnostic value of the measurements through a correlation of the  $(n,\gamma)/(n,2n)$  product ratio values with the downscattered neutron fraction measured by other means.

## II. Radioisotope production in the NIF chamber

The ICF capsules used in each experiment consisted of a 2-mm-diameter hollow-shell capsule of germanium-doped high-density plastic initially filled with a 50:50 mixture of deuterium and tritium gas at a pressure of 500-1000 Torr (DT fuel) and subsequently cooled to form DT ice in the capsule [8]. Each capsule was suspended centrally [9] in a cylindrical metal cavity (the hohlraum) and was maintained at a temperature near the triple point, approximately 19 K, so that a layer of DT ice, which contained most of the mass of the thermonuclear fuel, coated the inside of the shell [5]. The hohlraum, a cylinder roughly 0.6 cm in diameter, 1 cm long, and 30 mm thick (areal density of 0.06 g/cm<sup>2</sup>), was constructed of approximately 130 mg of gold, and sometimes contained a small amount of depleted uranium [10, 11]. High-Z materials have a high efficiency for conversion of incident laser light to x-rays, which drive the capsule implosion. The hohlraum matrix (gold and uranium) constituted the activation target for these

diagnostic measurements. The hohlraum was surrounded with a thermal-mechanical package of aluminum approximately 500 mm in thickness, which was held at the geometrical center of the 10-m-diameter NIF chamber at the end of a boom with clamps containing aluminum and silicon [12].

Each capsule was imploded by introducing up to 192 beams of 0.35-mm laser light [4, 13] through 0.31 cm laser entrance holes located at both ends of the hohlraum. Up to 1.8 MJ of energy was distributed over the inside surface of the hohlraum, which then absorbed the laser light and converted it to x-rays [1, 3]. There are inefficiencies associated with this conversion process meant to achieve a spherically symmetric implosion and, consequently, the fuel areal density. However, this technique is less susceptible to hydrodynamic instabilities that might be caused by minor deviations in the precise aiming of the lasers into the entrance holes than if the laser energy were focused directly on the capsule surface [14, 15, 16]. The photon energy and time distribution of laser power is tailored to provide an optimal x-ray environment in the hohlraum and to minimize backscattering of the incident laser light and the production of high-energy electrons that could heat the capsule fuel too early, thereby inhibiting compression of the fuel [17, 18, 19].

The x-ray bath inside of the hohlraum causes the outer surface of the capsule to ablate, which generates pressure and convergent shocks inside the capsule that compress the DT fuel with high velocity and minimum entropy to the temperatures and densities required for DT fusion. This in turn results in the production of neutrons, and the  $\rho R$  (areal density) of the capsule that determines the final energy spectrum [3, 14, 20] of the emitted neutrons. By the time the neutrons are produced, most of the plastic shell has ablated away, and the majority of the neutrons emerging at lower energies arise from scattering from the isotopes of hydrogen in the fuel together with a



significant contribution from the hydrogen in the remaining plastic ablator. Contributions from the low-density plasma that fills the hohlraum are negligibly small.

At maximum compression, the diameter of the hottest portion of the DT fuel (the hot spot) inside the capsule approaches 40  $\mu\text{m}$ , and  $\rho R$  approaches 1  $\text{g}/\text{cm}^2$  [21]. The time between the onset of the laser pulse and the production of neutrons is sufficiently short (nanoseconds) [22] that there is very little motion of the bulk gold hohlraum material from its initial position during that time, even though a few micrometers of its inner surface have been heated to hundreds of eV [14]. The neutrons arrive at the hohlraum and produce a variety of nuclear reaction products before the hohlraum matrix finally breaks apart and moves away from the center of the NIF chamber, thereby becoming target “debris.” Following neutron production, high-kinetic-energy ICF-capsule material stagnates against the hot inner wall of the hohlraum, launching shocks into the matrix. When the shocks break out of the outer surface of the hohlraum, much of the energy is radiated as part of the x-ray continuum, but the rest goes into kinetic energy of the debris [23]. This leads to atom-scale surface vaporization and larger-size ejecta, which propagate ballistically through the vacuum of the NIF chamber shortly after leaving the vicinity of the center of energy production [24, 25, 26, 27]. The majority of the hohlraum mass is expected to be directed axially outward [28, 29].

In these experiments, we suspended passive collector foils at a distance of 50 cm from the target chamber center (TCC) to collect the resultant capsule and hohlraum debris. These collectors were oriented near the plane of symmetry through the cylindrical waist of the hohlraum to maximize the collection of gold activation products. The collection process is complicated by the harsh environment found inside the NIF chamber following a shot, which includes scattered laser light, x rays, neutrons, and debris that

originated from material ablated from the chamber wall and diagnostic instruments fielded inside the chamber. Neutrons emitted by the DT fuel and x rays emitted by the hohlraum and thermal-mechanical package arrive at the collector position approximately 10 ns following the end of fusion-energy production. Debris arrives considerably later, on the order of microseconds to milliseconds depending on its particulate size and mass. The sub-keV x rays that dominate the spectrum of photons emitted by the hohlraum assembly deposit most of their energy within a few micrometers of the surface of high-melting point collector materials [30, 31].

Aluminum collectors, with a lower melting temperature, had melt depths of several tens of micrometers, though there was no correlation with laser power or distance from the target chamber center [32]. The x-ray pulse duration was short compared to the time required for heat transport [33], so surfaces were driven past their melting points (see reference 34, for example). The associated thermal shock caused material to ablate from the surface of the collector, which could impede the arrival of atom-scale debris. This problem is expected to be worse if the collector is moved from a waist, or equatorial, location to a polar location; the spectrum of radiation emitted through the laser entrance holes at the ends of the hohlraum was of higher energy [23, 25], which added significantly to the x-ray load of the collector. Gamma-ray spectroscopy analyses of the Au on the collector foils indicated clearly that the Au debris was not homogeneously distributed with respect to the pole and equator. These analyses also showed that the distribution of Au debris at the equatorial line-of-sight varied significantly for a given shot, with no dependence on the collector material, bracket position, or laser energy [30].



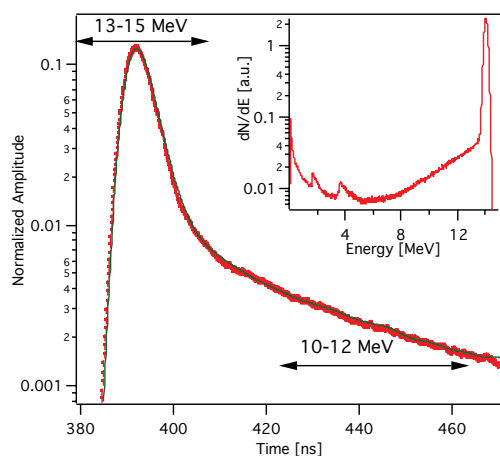


**Figure 29:** (a): Neutron Time-of-Flight spectrum from the equatorial nToF 20-meter detector for shot N120321-001-999. The red dots are data with error bars; the green is the fit to the data. Inset is the energy spectrum used to fit the data, from an MCNP simulation. The DSR inferred from this spectrum is  $0.050 \pm 0.004$  and the average over all lines-of-sight is  $0.060 \pm 0.004$ . This deviation from the average is consistent with a systematic low DSR on the equator for cryogenic fuel implosions.

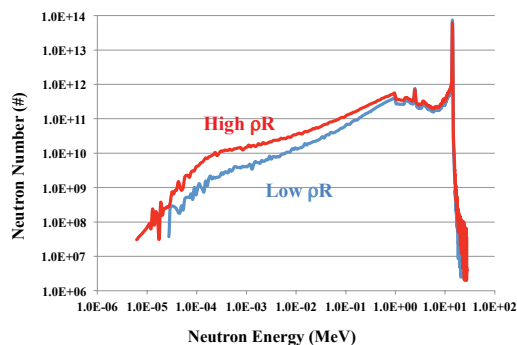


**Figure 29(b):** Post-shot analysis of the neutron number escaping the capsule boundary, plotted as a function of energy. The spectra are derived from NIF implosion experiments N111215 (Low- $\rho R$ ) and N120321 (High- $\rho R$ ), which had measured DSR values of 0.046 and 0.062 respectively. These DSR values correspond to DT areal densities of 0.92 and 1.24 g/cm<sup>2</sup>

The energy spectrum of neutrons that have passed through the hohlraum is measured at NIF by a variety of scintillator-based neutron Time-of-Flight (nToF) detectors and a magnetic recoil spectrometer (MRS) [36, 37]. A typical neutron Time-of-Flight spectrum is shown in Figure 29a, and typical derived neutron energy spectra for two  $\rho R$  values are shown in Figure 29b. One quantity that is derived from the measured spectra is the down-scattered

neutron ratio (DSR), which is used to infer the  $\rho R$  of the fuel. DSR is defined as the number of neutrons that have energies between 10 and 12 MeV (most of which have scattered only once) divided by the number of neutrons considered to be “unscattered,” with energies between 13 and 15 MeV. In this work the DSR of the capsule was obtained by fitting the neutron energy spectrum from the 20-meter neutron time-of-flight detectors and from the magnetic recoil spectrometer, 10 to 12 MeV and 13-15 MeV, respectively, and calculating the ratio. The authorized DSR value for each NIF shot is determined by performing a weighted average of DSR values from several neutron diagnostics.

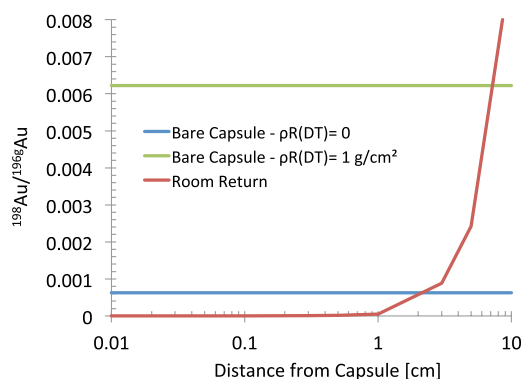


**Figure 30:** Calculated Au ratio from unscattered and room-return neutrons as a function of distance from the center of the NIF target chamber. The neutron source is a pure DT fusion spectrum at an ion temperature of approximately 3 keV. The expected Au ratio for 2 different values of  $\rho R(\text{DT})$  in units of g/cm<sup>2</sup> is also shown for comparison. A thin Au absorber with negligible neutron downscatter is assumed.

Neutrons emitted by the NIF capsule also encounter the NIF chamber wall and the various structural supports located relatively close to the center of fusion-energy production. The neutrons scattered off these materials bathe the region near the center of the NIF chamber with lower-energy “room-return” neutrons. Room-return neutrons include those resulting from (n,2n) reactions on local target support and diagnostic structures, as well as the more highly thermalized neutrons scattered from chamber walls and surrounding building materials.

The interaction of these neutrons with the hohlraum debris, mostly through  $(n,\gamma)$  reactions, must be assessed before the  $^{197}\text{Au}$   $(n,\gamma)$  products can be attributed primarily to the capture of neutrons that had previously down-scattered solely off the fuel in the compressed ICF capsule [38]. A Monte Carlo neutron transport calculation using MCNP5 with ENDF/BVII cross sections was performed to assess the contribution of room-return neutrons [39, 40]. The main components of the NIF target chamber and surrounding building were included in the Monte Carlo geometry. Isotropic DT fusion neutrons were injected at the center of the chamber and tracked until they either escaped or were captured in the building materials. Gold activation tallies were calculated at various radii from the center. The contribution from room return was evaluated by subtracting the activation by the bare capsule. Figure 30 shows the simulation results indicating that room-return neutrons make a negligible contribution to the Au ratio for distances  $< 1$  cm, even for low  $\rho R$  capsules. We performed the experiments described below to verify the results of these simulations.

### III. Neutron reactions on $^{197}\text{Au}$

The radioisotope inventory arising in fast-neutron interactions with  $^{197}\text{Au}$  is dominated by the products of  $(n,2n)$  and  $(n,\gamma)$  reactions, forming  $^{196}\text{Au}$  and  $^{198}\text{Au}$ , respectively. Both  $^{196}\text{Au}$  and  $^{198}\text{Au}$  have long-lived isomeric states that decay by internal conversion [41, 42, 43]. The 8.2-second first isomeric state in  $^{196}\text{Au}$  has completely decayed to the 6.2-day ground state before our radiometric measurements could be performed due to the length of time associated with retrieving collectors following a NIF shot; isotopic concentrations that we attribute to  $^{196g}\text{Au}$  are more accurately associated with the sum of those for  $^{196m1}\text{Au}$  and  $^{196g}\text{Au}$ . We refer to the higher-energy 9.6-hour isomeric state with

the short-hand designation  $^{196m}\text{Au}$  for the following discussions.

The  $^{197}\text{Au}(n,2n)$  reaction has a threshold of 8.1 MeV [44]. This means that scattered room-return neutrons are unlikely to contribute to the production of  $^{196}\text{Au}$ . For neutrons with energies in the vicinity of 14.1 MeV, the cross section for the production of  $^{196m+g}\text{Au}$  is 2200 mb [45] (see Figure 31). The target nuclide  $^{197}\text{Au}$  has  $J^\pi = 3/2^-$ ; the required spin change and the excitation energy of  $^{196m}\text{Au}$  strongly favors the production of the ground state. The average of literature values for the isomer ratio is  $\sigma(^{196m}\text{Au})/\sigma(^{196g}\text{Au}) = 0.069$  [46, 47, 48, 49], which is nearly identical to the value we obtained from our measurements (see results below).

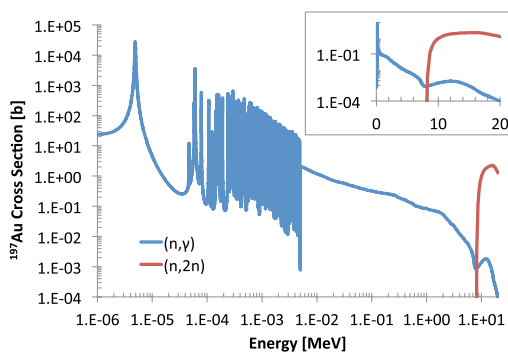


**Figure 31:**  $^{197}\text{Au}(n,2n)$  and  $^{197}\text{Au}(n,\gamma)$  evaluated cross sections from the Evaluated Nuclear Data File available through the National Nuclear Data Center at Brookhaven National Laboratory [62]. The insert figure has the Au cross sections with a linear scale for the neutron energy.

The  $^{197}\text{Au}(n,\gamma)$  reaction has no energy threshold; therefore, neutrons of all energies can produce  $^{198}\text{Au}$  (see Figure 31). Because of the similarity of the  $^{198}\text{Au}$  and  $^{196}\text{Au}$  nuclear structures, it may be possible that a similar isomer ratio would be obtained with 14-MeV-neutron capture as for the  $(n,2n)$  process. The  $^{197}\text{Au}(n,\gamma)$  cross section at 14 MeV is only 1 mb [38, 50, 51], yet we observe production of  $^{198}\text{Au}$  considerably in excess of that which would be produced with this cross section (see results below). We did not obtain any conclusive evidence for the production of  $^{198m}\text{Au}$  in the present experiments.

#### IV. Experimental details

Solid radiochemistry collectors (SRCs) to collect target debris were fielded in the NIF chamber on a fixed bracket mounted on the outside surface of a retractable diagnostic instrument manipulator (DIM) (see Figure 33). The distance between the center of the front surface of the collector disk and the center of the ICF capsule was 50 cm, with the line of sight being very nearly perpendicular to the surface of the disk. In several instances, trailing thin foils were mounted behind the collector so that they were not exposed to the chamber debris but were exposed to the neutron flux leaving the capsule plus the room-return neutrons. Each collector foil stack was backed up with a compression spring such that the collecting surface always registered against the retaining clamp at exactly the same distance from the ICF capsule.

A variety of materials with at least 99.9% purity were employed as collectors, including Ta, V, Ti, Nb, Mo, Ag and graphite foil; these were part of a systematic effort to determine the relative collection properties of the materials. Each collector was 5 cm in diameter and 1 mm thick, with the exception of the graphite foil, which was 0.1 mm thick and backed with a 0.5 mm thick piece of aluminum. A variety of surface finishes were also explored, and it was determined that polished surfaces with a roughness of  $\leq 1 \mu\text{m}$  rms variation were most effective in debris collection. The retaining ring that held the collector in position was stainless steel, with an opening that was 4 cm in diameter; while the entire volume of the collector foil was activated by the neutron exposure, only a 4-cm-diameter area centered on the front of the disk collected debris ( $4 \times 10^{-4}$  of  $4\pi$ ). There was little systematic advantage of any particular material over the others in the efficiency of debris collection [30], but Ta, V, and graphite foil provided the least interference with the detection of gamma rays emitted by the gold-hohlraum material. In some of the experiments whose results are given below, Ta collectors ( $\sim 1.7 \text{ g/}$

$\text{cm}^2$ ) were backed with an aluminum isolation foil, a gold disk, and a Ta disk, each 0.1 mm thick (see Figure 32); these trailing foils were designed to measure room-return neutrons. The cross section for the elastic scattering of fast neutrons by high-Z materials is on the order of a few barns, giving an inverse cross section of  $0.5 \text{ mole/cm}^2$ . A 1-mm-thickness of most metals is on the order of  $0.01 \text{ mole/cm}^2$ , so there are few down-scatter interactions of neutrons as they pass through the foil stack.

Samples were retrieved from the NIF chamber and were available for gamma-ray counting between 3 and 12 hours following the laser shot. The samples were wrapped in two layers of plastic to contain adsorbed tritium, which was present in the NIF chamber as unconsumed fuel from the ICF capsule. They were then mounted in standard aluminum or plastic counting fixtures, covered with precisely machined cadmium foils ( $0.4 \text{ g/cm}^2$ ) and placed at well-characterized locations in front of high-purity germanium coaxial photon detectors [52] in shielded enclosures. The purpose of the cadmium foils was to absorb the Pt x-rays emitted in the EC decay of  $^{196}\text{gAu}$  so that they would not sum in the detector material with the coincident gamma rays; for photons with energies above 100 keV, the attenuation was  $< 50\%$  [52]. The detectors had relative efficiencies between 20% and 40% of a reference sodium-iodide detector, NaI(Tl) [52]. The energy and efficiency calibrations were performed [54] with NIST-traceable radionuclide certified reference materials in accordance with the International Organization for Standardization (ISO) 17025 standard.

Each collector was counted several times over a span of three or more days. Initially, several 4-hour counts of each source were taken to characterize the intensities of the gamma rays emitted by 10-hour  $^{196\text{m}}\text{Au}$ . The source was placed no closer than 3 cm from the front face of the detector endcap in order to minimize coincident summing because a cascade of photons are emitted in the decay of

$^{196m}\text{Au}$ . Afterward, the source was moved 2 cm closer to the detector and counted to quantify the 2-day  $^{198g}\text{Au}$ , which does not suffer from summing. Two days after the shot, the source was backed off to its original position to quantify the 6-day  $^{196g}\text{Au}$ . In each case, the count rate in the detectors was sufficiently small that no correction was necessary for random summing.

Photon spectra between 50 keV and 2 MeV were collected in 4096 channels. The time base was corrected internally for dead time. The spectra were processed with LLNL's GAMANAL code [55, 56], which calculated the energy and intensity of each observed photon peak using the calibration parameters (including peak shape); it also corrected for extended source size and attenuation due to the presence of the plastic confinement layers, the cadmium absorber, and self-attenuation by the sample itself [53]. Uncertainties associated with the final photons/minute data were obtained from the statistical weights of the photopeaks and algorithms in the code taking into account photopeak efficiencies. In rare cases where a desired photopeak was insufficiently intense to be quantified by GAMANAL, its intensity and associated uncertainty were determined graphically. Each spectrum was processed through GAMANAL twice, once as a 5-cm-diameter x 1-mm-thick disk for the calculation of the intensities of activities induced by neutrons in the collector matrix, and a second time as a 4-cm-diameter by 1- $\mu\text{m}$ -thick disk for the calculation of the intensities of activities collected on the foil surface. The assumption of a 1- $\mu\text{m}$ -thick distribution of debris collection is based on measurements of the melt depth in cross-sectioned Ta and V collectors [30, 57]; the associated attenuation correction was a small addition to that for the Cd absorber. Based on the absolute count rates from the various collectors, there is evidence that the solid debris that emanates from the NIF capsule and hohlraum assembly is not distributed homogeneously in the lateral direction. We

therefore report isotope ratios as a means to mitigate the effects of uneven debris collection on the collector surfaces.

In the debris-collector spectra we routinely observed the photons emitted in the decays of  $^{196m}\text{Au}$ ,  $^{196g}\text{Au}$  and  $^{198g}\text{Au}$ . We also observed photons associated with interfering activities produced in the collector matrix itself, as well as  $^{24}\text{Na}$ , which we attribute to  $^{27}\text{Al}(n,\alpha)^{24}\text{Na}$  reactions in the thermal-mechanical package surrounding the hohlraum. We have no convincing evidence for the observation of  $^{198m}\text{Au}$ , and placed an upper limit of 0.11 to 0.13 on the  $^{198m}\text{Au}/^{198g}\text{Au}$  ratio for several representative samples. In the trailing gold foils we also detected  $^{196m}\text{Au}$ ,  $^{196g}\text{Au}$  and  $^{198g}\text{Au}$ . The limit on the production of  $^{198m}\text{Au}$  in these foils was  $N(^{198m}\text{Au})/N(^{198g}\text{Au}) \leq 0.002$ .

Photon intensity information from GAMANAL was converted to atoms at shot time using evaluated nuclear data [41, 42, 43]. The reference time associated with the intensity of each measured photopeak was near the centroid of the counting interval, corrected for the nonlinearity of the decay during that interval (finite-counting-time correction<sup>55</sup>). The photopeak intensities associated with each observed activity were calculated at the time of the shot assuming a single-component exponential decay. Several determinations of the initial concentrations of the same nuclide were propagated as a weighted average. We corrected the resulting initial atom concentration of  $^{196g}\text{Au}$  for contributions from the decay of  $^{196m}\text{Au}$  under the asymptotic assumption: by using  $^{196g}\text{Au}$  data taken after 48 hours of decay, given the isomer ratio from the literature, we can assume that the decay of  $^{196m}\text{Au}$  is sufficiently complete that simple exponential decay of  $^{196g}\text{Au}$  has been established (within 0.3%). Under this condition, the difference between the single-component extrapolation to shot time and the actual initial concentration of  $^{196g}\text{Au}$  is  $\lambda(^{196m}\text{Au})/[\lambda(^{196m}\text{Au}) - \lambda(^{196g}\text{Au})] \times N(^{196m}\text{Au})$ , or 1.0694 times the measured initial isomer concentration. We assumed that the production of  $^{198m}\text{Au}$  was

negligible, and made no correction for its decay contribution to the extrapolated initial concentration of  $^{198}\text{gAu}$ .

More than one collector foil was fielded on many of the ICF shots. The gamma-ray data from each collector were processed individually to derive an isotope ratio for that foil. The debris collection efficiency was quite variable among the foils. The uncertainties associated with the intensity of the photon lines emitted in the decay of the gold debris were dependent on the efficiency, the activation of the collecting medium, and the time required to recover the samples from the NIF target chamber and to mount them for counting. As a result, for each ICF shot, it was quite common that one sample yielded a  $N(^{198}\text{gAu})/N(^{196}\text{gAu})$  value (the isotope ratio) that was of significantly lower uncertainty than those yielded by the other collectors. Rather than propagate together all the isotope ratio values from one shot, we report the best value for an individual collector; the other values were treated as confirmatory and are not presented here.

The downscattered neutron ratio was determined from the neutron energy spectrum measured by two types of diagnostic devices. The first is neutron time-of-flight instruments [58] located approximately 20 m from the target chamber center and oriented in the equatorial and polar directions with respect to the hohlraum. These instruments detect the neutrons using a fast xylene scintillator with a low scintillation tail at greater than 40 ns after the main scintillation peak. The other neutron diagnostic device is a magnetic recoil spectrometer [59] that determines the neutron energy by measuring recoil protons produced by neutrons colliding with a thin plastic foil. These protons are magnetically analyzed and focused on a series of collectors that record the protons using Columbia Resin #39 (CR-39) film. The authorized DSR value for a particular laser shot is determined using the suite of neutron spectral measurement devices active on that shot. The number of

neutrons in the two energy bins is determined for each instrument and the ratio formed. The ratios from the active devices are averaged to determine the authorized DSR value.

## V. Results

From an MCNP simulation, we expected the correction for the contribution of room-return neutrons (neutrons thermalized through scatterings from the NIF experimental apparatus and the chamber walls) to the  $^{198}\text{Au}$  content of the hohlraum debris to be small. Before the shot, the average distance of the Au hohlraum is approximately 0.37 cm from the capsule and little motion is expected before burntime. From the results of Figure 30, we predict a small contribution from room return to the Au ratio. Nevertheless, we performed activation measurements to evaluate this conclusion guided by the calculation. In four cases in which a tantalum collector was employed, we backed the collector with thin foils of Au and Ta. These foils were retrieved and counted separately from the collector foil. Sections of representative spectra from one experiment are shown in Figure 33. All spectra were taken at approximately the same time with detectors of similar efficiencies. The top spectrum is associated with the trailing Au foil, and the bottom spectrum is a count of the debris collector (Au collected on Ta). From the comparison of the spectra, it is clear that the activation of Ta does not interfere with the detection and quantification of gold hohlraum debris.

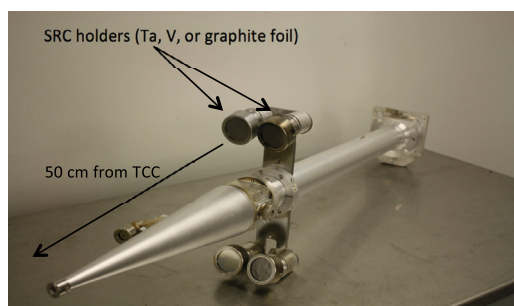


**Figure 32:** A picture of a diagnostic instrument manipulator (DIM) with four solid radiochemical collector (SRC) holders in place. The ICF target assembly at the target chamber center (TCC) is just beyond the end of the DIM, 50 cm from the SRC holders.

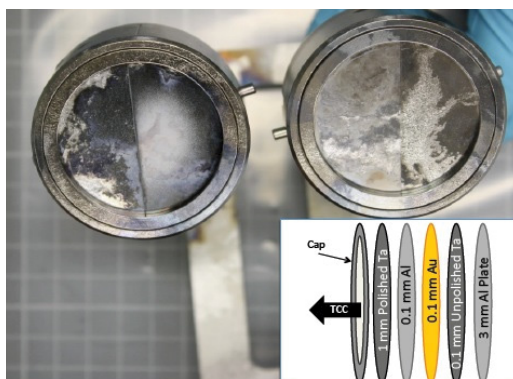


**Figure 33:** A post-shot picture and schematic drawing of the debris collectors, oriented toward the target chamber center (TCC), fielded in one of the NIF shots. The pre-shot collector foils were polished to a surface finish of less than 8 micrometers; the surface discoloration is due to the effects of NIF capsule radiation and debris. Each collector is typically 5 cm in diameter and 1 mm thick, with the exception of the graphite foil, which was 0.1 mm thick and backed with a 0.5 mm thick piece of aluminum.

Inspection of the top and bottom spectra in Figure 33 shows that there is a substantial contribution from the capture of room-return neutrons to the  $^{198}\text{Au}$  concentration in the trailing gold foil compared to that in the hohlraum material. Quantitatively, the measured  $N(^{198}\text{Au})/N(^{196}\text{Au})$  isotope ratio in the trailing foil is  $11 \pm 4$  times greater than in the hohlraum material. We assume that the room-return neutron field produced by scatter from the chamber walls and experimental fixtures and equipment in the chamber, which is incident on the trailing foil and the hohlraum material, is essentially the same for both because of their proximity in the

large NIF chamber. However, the exposure to neutrons produced in the capsule decreases with the square of the distance from the capsule. The hohlraum is on the order of 1 cm from the capsule when the fusion neutrons arrive, while the trailing foil is 50 cm from the capsule. Thus we approximate that the room-return neutrons contribute about  $11/2500$ , or less than 1%, to the production of  $^{198}\text{Au}$  in the hohlraum debris. As a result, we assess the measured  $N(^{198}\text{Au})/N(^{196}\text{Au})$  isotope ratio in the debris as arising from the interaction of the capsule neutron output with the gold-hohlraum matrix without significant contribution from room return.

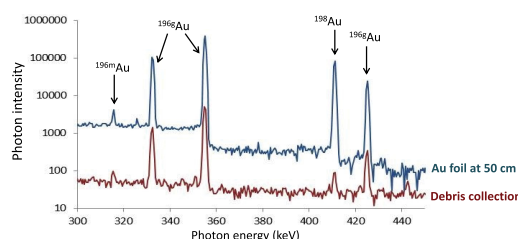


**Figure 34:** Spectra of gamma rays from hohlraum gold debris from a representative NIF shot.

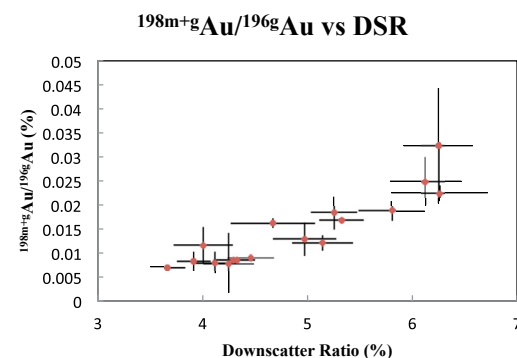


**Figure 35:** A plot of the Au isotope ratio  $N(^{198m+g}\text{Au})/N(^{196}\text{Au})$  versus the DSR value from seventeen NIF shots fielded between January 2012 and March 2013. One sigma error bars are plotted.

In Figure 34 we present the results of our radiochemical measurements of the  $N(^{198}\text{Au})/N(^{196}\text{Au})$  ratios (the isotope ratio) from debris collectors from eighteen ICF shots fielded between January 2012 and March 2013 (no measurement was obtained for one shot), correlated with the authorized DSR



value associated with each experiment. The  $N(^{196m}\text{Au})/N(^{196g}\text{Au})$  ratio (the isomer ratio) has been measured for the same eighteen ICF shots utilizing Au spectroscopic data from hohlraum debris collected near the equatorial plane. The data are summarized in Figure 35 along with isomer ratios reported in the literature. The literature values vary considerably, ranging from a 5.9% to 7.9%, with an overall average of 6.9%. The isomer ratios obtained from the Au samples produced via irradiation from the ICF capsule neutron spectrum are consistent with each other within their statistical accuracy, and an overall weighted average of  $7.05\% \pm 0.04\%$  (statistical)  $\pm 0.28\%$  (systematic) is obtained.

## VI. Discussion

The ratio of  $^{197}\text{Au}(n,\gamma)$  and  $^{197}\text{Au}(n,2n)$  cross sections at 14 MeV is approximately  $5 \times 10^{-4}$  (see Figure 2). We observe that in each measurement the  $N(^{198g}\text{Au})/N(^{196g}\text{Au})$  value is in excess of this, demonstrating the contribution to  $^{198g}\text{Au}$  production from capsule neutrons at energies well below 14 MeV. Figure 34 demonstrates that the correlation between the gold isotope ratio and the DSR is monotonically increasing, though not linear, since for a monoenergetic 14-MeV neutron spectrum the isotope ratio at DSR = 0 should be approximately  $5 \times 10^{-4}$ . The non-linearity of the Au isotope ratio data is not surprising because the DSR is a measure of neutrons that have undergone a very limited number of scattering interactions, while the production of the  $^{198g}\text{Au}$  component of the gold isotope ratio is strongly influenced by exposure to more highly scattered neutrons (see Figure 30). Despite this observation, the Au isotope ratio versus DSR value can be represented approximately by a straight line over the present range of the data.

The DSR and Au ratio provide information about compression ( $\rho R$ ) of the fuel (DT) and ablator (CH) capsule constituents during burn.

Nuclear cross sections at  $E = 14$  MeV show that for a given  $\rho R$ , the DSR contribution from DT is about 4 times that of CH. By contrast, DT and CH are approximately equally effective in increasing the Au ratio through neutron downscattering. A given pair of DSR and Au ratio values can therefore be used to uniquely determine both  $\rho R(\text{DT})$  and  $\rho R(\text{CH})$  at burn time. Details of the analysis and application to NIF data will be given in a separate publication [40].

The Au isomer ratios,  $N(^{196m}\text{Au})/N(^{196g}\text{Au})$ , from the individual shots are consistent with each other within the uncertainties of the measurement, as well as the extant literature data (see Figure 35). There is no significant dependence of the values on the 14-MeV neutron yield or DSR for these data obtained from collectors located equatorially. The weighted average obtained,  $7.05\% \pm 0.04\% \pm 0.28$  (systematic), is in good agreement with the isomer ratios determined from accelerator-based measurements. Experiments such as these at the NIF have an advantage that all radioactive species are produced at essentially the same instant.

The success of these nuclear isotope and isomer ratio measurements at the NIF suggests that the facility can be used for studies in basic nuclear physics and astrophysics. The fuel in an ICF capsule is driven to temperatures and pressures comparable with those found in the interiors of Asymptotic Giant Branch (AGB) stars, low- to medium-mass stars where the s-process is thought to occur. This nucleosynthesis process occurs over a long time period by capture of neutrons generated by the nuclear reactions in the star. Depending on the mass, composition, and stage of evolution of the AGB star, the s-process produces elements heavier than Fe up to Y and Sr, even up to Pb under some conditions. These heavy elements can be ejected into the interstellar medium by a supernova explosion.

Although the neutron spectrum produced by an ICF capsule is dominated by 14-MeV neutrons (see Figure 29a and Figure 29b), there can be a significant contribution from neutrons that mimic those that produce heavy elements via



the s-process [60, 61, 62]. In addition, since the thermal environment during the ICF implosion is elevated, the potential exists to measure cross sections of nuclei with excited levels in thermal equilibrium, an interesting complement to experiments at accelerator laboratories where targets are at ambient temperature.

Mounting collection assemblies with trailing foils at more than one distance from the NIF target-chamber center can be used to distinguish that fraction of an induced isotope inventory due to room return from that arising directly from the capsule. If the spectrum of room-return neutrons can be characterized, intensities are such that radiochemical measurements of cross sections for  $(n,\gamma)$  reactions at intermediate energies can be proposed.

In summary, measurements of the neutron activation of Au in the hohlraum of the NIF ICF capsules have been performed to demonstrate the usefulness of these measurements to diagnose ICF implosions, as well as to measure neutron cross sections, or cross section ratios. Furthermore, since the ICF implosions occur at temperatures comparable to those in stars, the possibility to use NIF to measure astrophysically important neutron cross sections of importance to astrophysics is suggested by the present work.

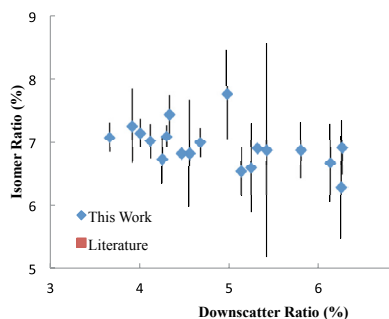


**Figure 36:** A plot of the Au isomer ratios obtained from eighteen NIF shots versus the neutron downscatter ratio. The weighted average of the values is  $7.05\% \pm 0.04\% \pm 0.28$  (systematic). One sigma statistical uncertainties are shown. Also shown are the results of accelerator-based experiments taken from the literature [46-49].

## VII. References

- [1] J.H. Nuckolls, *Phys. Today* **35**, 24 (Sept. 1982).
- [2] J. Nuckolls, L. Wood, A. Thiessen and G. Zimmerman, *Nature* **239**, 139 (1972).
- [3] J. Lindl, *Phys. Plasmas* **2**, 3933 (1995).
- [4] E.I. Moses, R.N. Boyd, B.A. Remington, C.J. Keane and R. Al-Ayat, *Phys. Plasmas* **16**, 041006 (2009).
- [5] J.K. Hoffer and L.R. Foreman, *Phys. Rev. Lett.* **60**, 1310 (1988).
- [6] R.F. Post, *Ann. Rev. Nucl. Sci.* **20**, 509 (1970).
- [7] V. McLane, C.L. Dunford and P.F. Rose, "Neutron cross sections, volume 2, neutron cross section curves", Academic Press, Boston (1988).
- [8] S. W. Haan, J. D. Lindl, D. A. Callahan, D. S. Clark, J. D. Salmonson, B. A. Hammel, L. J. Atherton, R. C. Cook, M. J. Edwards, S. Glenzer, A. V. Hamza, S. P. Hatchett, M. C. Herrmann, D. E. Hinkel, D. D. Ho, H. Huang, O. S. Jones, J. Kline, G. Kyrala, O. L. Landen, B. J. MacGowan, M. M. Marinak, D. D. Meyerhofer, J. L. Milovich, K. A. Moreno, E. I. Moses, D. H. Munro, A. Nikroo, R. E. Olson, K. Peterson, S. M. Pollaine, J. E. Ralph, H. F. Robey, B. K. Spears, P. T. Springer, L. J. Suter, C. A. Thomas, R. P. Town, R. Vesey, S. V. Weber, H. L. Wilkens, and D. C. Wilson, *Phys. of Plasmas*, **18**, 0551001 (2011).
- [9] S.O. Kucheyev and A.V. Hamza, *J. Appl. Phys.* **108**, 091101 (2010).
- [10] H.L. Wilkens, A. Nikroo, D.R. Wall and J.R. Wall, *Phys. Plasmas* **14**, 056310 (2007).
- [11] O.S. Jones, J. Schein, M.D. Rosen, L.J. Suter, R.J. Wallace, E.L. Dewald, S.H. Glenzer, K.M. Campbell, J. Gunther, B.A. Hammel, O.L. Landen, C.M. Sorce, R.E. Olson, G.A. Rochau, H.L. Wilkens, J.L. Kaae, J.D. Kilkenny, A. Nikroo and S.P. Regan, *Phys. Plasmas* **14**, 056311 (2007).
- [12] G.J. Laughon and K.R. Schultz, *Fusion Technol.* **30**, 471 (1996).
- [13] R.S. Craxton, *Optics Commun.* **34**, 474 (1980).
- [14] J.D. Lindl, "Inertial Confinement Fusion, The Quest for Ignition and Energy Gain Using Indirect Drive" (AIP Press/Springer-Verlag, New York, 1998).
- [15] J.D. Lindl, P. Amendt, R.L. Berger, S.G. Glendinning, S.H. Glenzer, S.W. Haan, R.L. Kauffman, O.L. Landen and L.J. Suter, *Phys. Plasmas* **11**, 339 (2004).
- [16] B.A. Remington, S.V. Weber, S.W. Haan, J.D. Kilkenny, S.G. Glendinning, R.J. Wallace, W.H. Goldstein, B.G. Wilson and J.K. Nash, *Phys. Fluids* **B5**, 2589 (1993).
- [17] T. Chang, J. Sheng, W. Miao, Y. Li, S. Jiang, W. Pei, J. Chen, Y. Gao, J. Yang, T. Feng, Z. Zheng, L. Zhang, Y. Ding, J. Li and M. Li, *Phys. Plasmas* **13**, 022704 (2006).
- [18] L. Suter, J. Rothenberg, D. Munro, B. van Wousterghem and S. Haan, *Phys. Plasmas* **7**, 2092 (2000).
- [19] K.A. Brueckner and S. Jorna, *Rev. Mod. Phys.* **46**, 325 (1974).
- [20] S.E. Bodner, *J. Fusion Energy* **1**, 221 (1981).
- [21] A.J. Mackinnon, J.L. Kline, S.N. Dixit, S.H. Glenzer, M.J. Edwards, D.A. Callahan, N.B. Meezan, S.W. Haan, J.D. Kilkenny, T. Döppner, D.R. Farley, J.D. Moody, J.E. Ralph, B.J. MacGowan, O.L. Landen, H.F. Robey, T.R. Boehly, P.M. Celliers, J.H. Eggert, K. Krauter, G. Frieders, G.F. Ross, D.G. Hicks, R.E. Olson, S.V. Weber,

- B.K. Spears, J.D. Salmonsens, P. Michel, L. Divol, B. Hammel, C.A. Thomas, D.S. Clark, O.S. Jones, P.T. Springer, C.J. Cerjan, G.W. Collins, V.Y. Glebov, J.P. Knauer, C. Sangster, C. Stoeckl, P. McKenty, J.M. McNaney, R.J. Leeper, C.L. Ruiz, G.W. Cooper, A.G. Nelson, G.G. Chandler, K.D. Hahn, M.J. Moran, M.B. Schneider, N.E. Palmer, R.M. Bionta, E.P. Hartouni, S. LePape, P.K. Patel, N. Izumi, R. Tommasini, E.J. Bond, J.A. Caggiano, R. Hatarik, G.P. Grim, F.E. Merrill, D.N. Fittinghoff, N. Guler, O. Drury, D.C. Wilson, H.W. Herrmann, W. Stoeffl, D.T. Casey, M.G. Johnson, J.A. Frenje, R.D. Petrasso, A. Zylestra, H. Rinderknecht, D.H. Kalantar, J.M. Dzenitis, P. Di Nicola, D.C. Eder, W.H. Courdin, G. Gururangan, S.C. Burkhart, S. Friedrich, D.L. Blueuel, L.A. Bernstein, M.J. Eckart, D.H. Munro, S.P. Hatchett, A.G. Macphee, D.H. Edgell, D.K. Bradley, P.M. Bell, S.M. Glenn, N. Simanovskaia, M.A. Barrios, R. Benedetti, G.A. Kyrala, R.P. Town, E.L. Dewald, J.L. Milovich, K. Widmann, A.S. Moore, G. LaCaille, S.P. Regan, L.J. Suter, B. Felker, R.C. Ashabraner, M.C. Jackson, R. Prasad, M.J. Richardson, T.R. Kohut, P.S. Datte, G.W. Krauter, J.J. Klingman, R.F. Burr, T.A. Land, M.R. Hermann, D.A. Latray, R.L. Saunders, S. Weaver, S.J. Cohen, L. Berzins, S.G. Brass, E.S. Palma, R.R. Lowe-Webb, G.N. McHalle, P.A. Arnold, L.I. Lagin, C.D. Marshall, G.K. Brunton, D.G. Mathisen, R.D. Wood, J.R. Cox, R.B. Ehrlich, K.M. Knittel, M.W. Bowers, R.A. Zacharias, B.K. Young, J.P. Holder, J.R. Kimbrough, T. Ma, K.N. La Fortune, C.C. Widmayer, M.J. Shaw, G.V. Erbert, K.S. Jancaitis, J.M. DiNicola, C. Orth, G. Heestand, R. Kirkwood, C. Haynam, P.J. Wegner, P.J. Whitman, P.K. Hamza, A. Dzenitis, E.G. Wallace, R.J. Bhandarkar, S.D. Parham, T.G. Dylla-Spears, R. Mapoles, B.J. Kozioziemski, J.D. Sater, C.F. Walters, B.J. Haid, J. Fair, A. Nikroo, E. Giraldez, K. Moreno, B. Vanwonterghem, R.L. Kauffman, S. Batha, D.W. Larson, R.J. Fortner, D.H. Schneider, J.D. Lindl, R.W. Patterson, L.J. Atherton, E.I. Moses, *Phys. Rev. Lett.* **108**, 215005 (2012).
- [22] H.W. Herrmann, N. Hoffman, D.C. Wilson, W. Stoeffl, L. Dauffy, Y.H. Kim, A. McEvoy, C.S. Young, J.M. Mack, C.J. Horsfield, M. Rubery, E.K. Miller and Z.A. Ali, *Rev. Sci. Instrum.* **81**, 10D333 (2010).
- [23] A.T. Anderson, R.A. Managan, M.T. Tobin and P.F. Peterson, *Fusion Technol.* **30**, 425 (1996).
- [24] B.E. Blue, J.F. Hansen, M.T. Tobin, D.C. Eder and H.F. Robey, *Rev. Sci. Instrum.* **75**, 4775 (2004).
- [25] D. Eder, A. Koniges, F. Bonneau, J. Vienne, P. Combis, M. Tobin, J. Andrews, K. Mann and B. MacGowan, "Simulation of shrapnel to aid in the design of NIF/LMJ target-diagnostic configurations", in B. A. Hammel, D. D. Meyerhofer, J. Meyer-ter-Vehn and H. Azechi, editors, "Inertial Fusion Sciences and Applications 2003" (American Nuclear Society, La Grange Park, IL, 2004), p. 572.
- [26] F.E. Irons and N.J. Peacock, *J. Phys.* **B7**, 2084 (1974).
- [27] M. Dombrowski and W.R. Jones, *Chem. Engineering Sci.* **18**, 203 (1963).
- [28] D.C. Eder, A.E. Koniges, O.S. Jones, M.M. Marinak, M.T. Tobin and B.J. MacGowan, "Late-time simulation of National Ignition Facility hohlraums", *Nucl. Fusion* **44**, 709 (2004).
- [29] D.C. Eder, A.E. Koniges, O.L. Landen, N.D. Masters, A.C. Fisher, O.S. Jones, T.I. Suratwala and L.J. Suter, "Debris and shrapnel mitigation procedure for NIF experiments", *J. Phys. Conf. Ser.* **112**, 032023 (2008).

- [30] J.M. Gostic, D.A. Shaughnessy, K.T. Moore, I.D. Hutcheon, P.M. Grant, and K.J. Moody, *Rev. Sci. Instrum.* **83**, 10D904 (2012).
- [31] J.H. Hubbell and S.M. Seltzer, “Tables of X-Ray Mass Attenuation Coefficients and Mass Energy-Absorption Coefficients” (version 1.4). Online Available: <http://physics.nist.gov/zaamdi> [2004, July 12] National Institute of Standards and Technology, Gaithersburg, MD.
- [32] J.M. Gostic, “Development of Radiochemical Diagnostics at NIF Through Collection of Solid and Gaseous Debris”, JINA Workshop-Nuclear Physics in Hot Dense Dynamics Plasmas (London, 2011), LLNL-PRES-471281.
- [33] Y.S. Touloukian, R.W. Powell, C.Y. Ho and M.C. Nicolaou, “Thermal Diffusivity” (IFI/Plenum, New York, 1973).
- [34] A.M. Hassanein, H.M. Attaya, and G.L. Kulcinski, *Journ. Nucl. Mat.* **141-143**, 221 (1986).
- [35] D.C. Eder, R.W. Anderson, D.S. Bailey, P. Bell, D.J. Benson, A.L. Bertozzi, W. Bittle, D. Bradley, C.G. Brown, T.J. Clancy, H. Chen, J.M. Chevalier, P. Combis, L. Dauffy, C.S. Debonnel, M.J. Eckart, A.C. Fisher, A. Geille, V.Y. Glebov, J. Holder, J.P. Jadaud, O. Jones, T.B. Kaiser, D. Kalantar, H. Khater, J. Kimbrough, A.E. Koniges, O.L. Landen, B.J. MacGowan, N.D. Masters, A. MacPhee, B.R. Maddox, M. Meyers, S. Osher, R. Prasad, D. Raffestin, J. Raimbourg, V. Rekow, C. Sangster, P. Song, C. Stoeckl, M.L. Stowell, J.M. Teran, A. Throop, R. Tommasini, J. Vierne, D. White and P. Whitman, *J. Phys. Conf. Ser.* **244**, 032018 (2010).
- [36] J.A. Frenje, D.T. Casey, C.K. Li, F.H. Sequin, R.D. Petrasso, V.Yu. Glebov, P.B. Radha, T.C. Sangster, D.D. Meyerhofer, S.P. Hatchett, S.W. Haan, C.J. Cerjan, O.L. Landen, K.A. Fletcher and R.J. Leeper, *Phys. Plasmas* **17**, 056311 (2010).
- [37] R.A. Lerche, V.Yu. Glebov, M.J. Moran, J.M. McNaney, J.D. Kilkenny, M.J. Eckart, R.A. Zacharias, J.J. Haslam, T.J. Clancy, M.F. Yeoman, D.P. Warwas, T.C. Sangster, C. Stoeckl, J.P. Knauer and C.J. Horsfield, *Rev. Sci. Instrum.* **81**, 10D319 (2010).
- [38] D. Drake, I. Bergqvist and D.K. McDaniels, *Phys. Lett.* **B36**, 557 (1971).
- [39] “MCNP—A General N-Particle Transport Code, Volume 5”, X-5 Monte Carlo Team, LA-UR-03-1987 (2003, updated 2008).
- [40] C.A. Hagmann, to be published.
- [41] H. Xiaolong, *Nucl. Data Sheets* **110**, 2533 (2009).
- [42] H. Xiaolong, *Nucl. Data Sheets* **108**, 1093 (2007).
- [43] R.B. Firestone and V.S. Shirley, eds., “Table of Isotopes, 8<sup>th</sup> edition”, volume 2, John Wiley and Sons, New York (1996).
- [44] G. Audi, O. Bersillon, J. Blachot and A.H. Wapstra, *Nucl. Phys.* **A729**, 3 (2003).
- [45] B.P. Bayhurst, J.S. Gilmore, R.J. Prestwood, J.B. Wilhelmy, N. Jarmie, B.H. Erkkila and R.A. Hardekopf, *Phys. Rev.* **C12**, 451 (1975).
- [46] R.J. Prestwood and B.P. Bayhurst, *Phys. Rev.* **121**, 1438 (1961).
- [47] W. Dilg, H. Vonach, G. Winkler and P. Hille, *Nucl. Phys.* **A118**, 9 (1968).
- [48] G.N. Flerov, Yu.P. Gangrskii, B.N. Markov, A.A. Pleve, S.M. Polikanov and Kh. Yungklaussen, *Sov. J. Nucl. Phys.* **6**, 12 (1968).
- [49] R.B. Ryves and P. Kolkowski, *J. Phys.* **G7**, 115 (1981).
- [50] G. Magnussen, P. Andersson and I. Bergqvist, *Phys. Scripta* **21**, 21 (1980).
- [51] O. Schwerer, M. Winkler-Rohatsch, H. Warhanek and G. Winkler, *Nucl. Phys.* **A264**, 105 (1976).

- [52] G.F. Knoll, "Radiation detection and measurement", 3<sup>rd</sup> ed. (Wiley, New York, 2000).
- [53] C.M. Davisson, "Interaction of Gamma-Radiation with Matter", in "Alpha-, Beta- and Gamma-Ray Spectroscopy", ed. K. Siegbahn (North-Holland, Amsterdam, 1965), Chapter II.
- [54] FSC-SOP-26 rev. 4(LLNL-TM-427812) "Nuclear Counting Facility Detector Calibration Procedure for the Forensic Science Center".
- [55] R. Gunnink and J.B. Niday, "Computerized quantitative analysis by gamma-ray spectrometer", Lawrence Livermore Laboratory report UCRL-57061 (1971).
- [56] R. Gunnink and J.B. Niday, in "ERDA symposium on X- and gamma-ray sources and applications ",(U. S. Energy Research and Development Administration, CONF-760539, Washington, DC., GPO, 1976).
- [57] J.M. Gostic, personal communication.
- [58] Z.A. Ali, V.Yu. Glebov, M. Cruz, T. Duffy, C. Stoeckl, S. Roberts, T.C. Sangster, R. Tommasini, A. Throop, M. Moran, L. Dauffy, and C. Horsfield, *Rev. Sci. Instrum.* **79**, 10E527 (2008).
- [59] J. A. Frenje, D. T. Casey, C. K. Li, J. R. Rygg, F. H. Seguin, R. D. Petrasso, V. Y. Glebov, D. D. Meyerhofer, T. C. Sangster, S. Hatchett, S. Haan, C. Cerjan, O. Landen, M. Moran, P. Song, D. C. Wilson and R. J. Leeper, *Review of Scientific Instruments* **79** (10), 10E502 (2008).
- [60] M. Busso, R. Gallino and G.J. Wasserberg, *Ann. Rev. Astron. Astrophys.* **37**, 239 (1999).
- [61] F. Kaeppler, R. Gallino, S. Bisterzo and A. Wako, *Rev. Mod. Phys.* **83**, 157 (2011).
- [62] V. Trimble, *Rev. Mod. Phys.* **47**, 877 (1975).
- [63] M.B. Chadwick, M. Herman, P. Obložinský, M.E. Dunn, Y. Danon, A.C. Kahler, D.L. Smith, B. Pritychenko, G. Arbanas, R. Arcilla, R. Brewer, D.A. Brown, R. Capote, A.D. Carlson, Y.S. Cho, H. Derrien, K. Guber, G.M. Hale, S. Hoblit, S. Holloway, T.D. Johnson, T. Kawano, B.C. Kiedrowski, H. Kim, S. Kunieda, N.M. Larson, L. Leal, J.P. Lestone, R.C. Little, E.A. McCutchan, R.E. MacFarlane, M. MacInnes, C.M. Mattoon, R.D. McKnight, S.F. Mughabghab, G.P.A. Nobre, G. Palmiotti, A. Palumbo, M.T. Pigni, V.G. Pronyaev, R.O. Sayer, A.A. Sonzogni, N.C. Summers, P. Talou, I.J. Thompson, A. Trkov, R.L. Vogt, S.C. van der Marck, A. Wallner, M.C. White, D. Wiarda, P.G. Young, *Nuclear Data Sheets* **112**, 2887 (2011).



# FY2013 NIF Shots- Summary Table

Program	Campaign/Sub-campaign	Q1	Q2	Q3	Q4	Total
SSP-HED		18	20	25	23	86
	Burn Physics/DIME	4	2	2		8
	Code Validation/High-foot	3	4	6	7	20
	HED Drive & Coupling	1	2	1		4
	Alternate Ablator (Planar Ablator)		2	1		3
	Crystal Ball	1				1
	Hohlraum Physics	3	1	2		6
	Viewfactor		1			1
	Laser Entrance Hole Closure	3		2		5
	Hydrodynamics	3	4	7	6	20
	CD Mix	2	2	5	2	11
	LANL-Shock/Shear				1	1
	Toto (Complex Hydrodynamics)	1	2	2	3	8
	Material Properties	2	3	3	5	13
	Diffraction				3	3
	EOS		2	2		4
	Strength	2	1	1	2	6
	Mix Physics/HGR			4	4	8
	Radiation Transport	2	4		1	7
	LANL-Fanbolt		1		1	2
	LANL-Pleiades	2	3			5
SSP-ICF		19	26	15	12	72
	Plastic (CH) Ablator	12	15	4		31
	High Density Carbon (HDC) Ablator		1	3	8	12
	Hohlraum Physics		1	1		2
	Polar Direct Drive	1	1		2	4
	Implosion Shape	6	7	6	2	21
	Shock Physics/Shock Timing		1	1		2
Fundamental Science			4		3	7
	Ablative Rayleigh-Taylor		1			1
	Diffraction				1	1
	EOS: Fe		2			2
	EOS: Gbar		1		2	3
Natl. Security Applications		2	2		0	4
	Energy Partition/Energy Coupling (EPEC)	2	2			4
Diagnostics and Systems Qualification		10	16	11	3	40
Subtotal- Target Shots		49	68	51	41	209
Laser Performance		22	22	49	35	128
Grand Total		71	90	100	76	337

Figure 37: Chart Figure 1 TK.



